1

Cubic Silicon Carbide: Growth, Properties, and Electrochemical Applications

Nianjun Yang and Xin Jiang

Institute of Materials Engineering, University of Siegen, Paul-Bonatz-Str. 9-11, 57076 Siegen, Germany

1.1 General Overview of Silicon Carbide

It is well known that carbon and silicon atoms form similar, covalently bonded and giant structures, as shown schematically in Figure 1.1a. They are thus called carbon diamond and silicon diamond. In both diamond structures, each atom is covalently bonded to four other atoms located at the corner of a tetrahedron. Another diamond-like compound is silicon carbide (SiC), building up with silicon and carbon atoms. In this crystal, each atom is sp^3-hybridized and forms four bonds to four other atoms of the opposite kind. The tetrahedral arrangement of atoms encountered in the pure carbon and silicon diamond structures is preserved in SiC (Figure 1.1a).

The existence of a compound containing SiC bonds was proposed in 1824 for the first time by Jöns Jacob Berzelius, a Swedish chemist [1]. In 1905, Henri Moissan, a French chemist and the Nobel laureate, discovered SiC in nature [2]. In mineralogy, SiC is therefore known as moissanite [3]. In nature, moissanite SiC is very rare and only found in certain types of meteorite. The most commonly encountered SiC material is actually man-made.

SiC exists in about 250 crystalline forms, as variations of the same chemical compound that are identical in two dimensions but differ in the third. They can be viewed as layers stacked in a certain sequence. Different stacking sequences of C-Si double layers lead to different crystalline structures, or so-called polytypes [4]. Therefore, more than 250 polytypes have been predicted [4, 5]. Of these polytypes, only a few of them have been studied in detail. In principle, only three are of major importance: cubic (3C, or β)-SiC, 4H-SiC, and 6H(α)-SiC, which are shown schematically in Figure 1.1b–d, respectively. The most commonly encountered polymorph is 6H(α)-SiC, which forms at temperatures higher than 1700°C and has a hexagonal crystal structure (similar to wurtzite) (Figure 1.1c). Cubic 3C(β)-SiC (Figure 1. 1b) is formed at temperatures below 1700°C and has a zincblende (ZnS) crystal structure, similar to diamond [6].

1.1.1 SiC Properties

SiC is a fascinating material, although it has quite complicated polytypes. This is because the type of SiC polytype implies a corresponding set of relevant physical properties.

Novel Carbon Materials and Composites: Synthesis, Properties and Applications, First Edition.
Edited by Xin Jiang, Zhenhui Kang, Xiaoning Guo and Hao Zhuang.

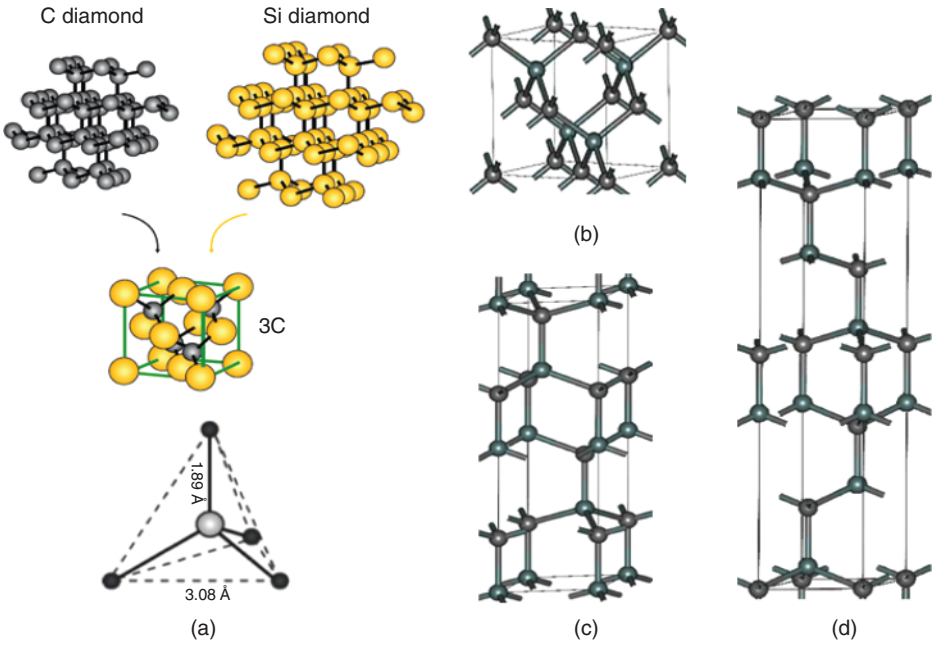

Figure 1.1 Chemical structures of carbon diamond, silicon diamond, SiC (a), 3C(β)-SiC (b), 4H-SiC (c), and 6H(α)-SiC (d) using ball-stick models.

As examples, some important physical properties of 4H-, 6H-, and 3C-SiC are listed in Table 1.1, compared with those of diamond and silicon.

SiC has been known for decades to be a semiconductor, based on the very first electroluminescence (yellowish light) from SiC crystals when subjected to electricity in 1907 [7]. More interestingly, its indirect bandgap is tunable in the range of 2.36–3.23 eV, determined by the polytype of SiC films. For instance, the bandgaps for 3C-, 4H-, and 6H-SiC are 2.36, 3.23, and 3.05 eV, respectively. However, SiC can be varied from insulating, semiconductive, to metallic-like in its properties when the dopants (n- or p-type) and the doping levels are altered. For example, SiC films can be doped with either n-type dopants (e.g. nitrogen, phosphorus) or p-type dopants (e.g. beryllium, boron, aluminum, gallium). Metallic conductivities of SiC films have been achieved by their heavy doping with boron, aluminum, or nitrogen. For example, at the same temperature of 1.5 K, superconductivity has been detected in 3C-SiC films doped with aluminum and boron as well as in 6H-SiC films doped with boron.

In comparison with Si, SiC has a higher thermal conductivity, electric field breakdown strength, and current density. It features a very low coefficient of thermal expansion (4.0×10^{-6} K^{-1}) and experiences no phase transitions that cause discontinuities in thermal expansion. The sublimation temperature of SiC is very high (approximately 2700°C), which makes it useful for bearings and furnace parts. SiC does not melt at any known temperature.

SiC is transparent to visible light. Pure SiC is colorless. The brown to black color of industrial SiC products results from iron impurities. The rainbow-like lusters of SiC crystals are caused by the passivation layers of SiO_2 that form on the SiC surface.

Table 1.1 Basic properties of three kinds of SiC, Si, and diamond.

Property	4H-SiC	6H-SiC	3C-SiC	Si	Diamond
Energy bandgap at 300 K (eV)	3.20	3.00	2.29	1.12	5.45
Intrinsic carrier concentration at 300 K (cm^{-3})	5×10^{-9}	1.6×10^{-6}	1.5×10^{-1}	1×10^{10}	$\sim 10^{-27}$
Critical breakdown electric field (MV cm^{-1})	2.2	2.5	2.12	0.25	1–10
Saturated electron drift velocity ($\times 10^7$ cm s^{-1})	2.0	2.0	2.5	1.0	1.5
Electron mobility (cm^2 V^{-1} s^{-1})	1000	600	800	1450	480
Electron mobility (cm^2 V^{-1} s^{-1})	115	100	40	470	1600
Thermal conductivity at 300 K (W cm^{-1} K^{-1})	3.7	3.6	3.6	1.49	6–20
Coefficient of thermal expansion at 300 K (10^{-6} K^{-1})	4.3 4.7	4.3 4.7	3.2	3.0	1.0
Lattice coefficient (a, c in Å)	a = 3.073 c = 10.053	a = 3.081 c = 15.117	a = 4.360	a = 5.430	a = 3.567
Calculated elastic coefficient (GPa)	$C_{44} = 600$	$C_{11} = 500$ $C_{12} = 92$ $C_{44} = 168$	$C_{11} = 352$ $C_{12} = 12$ $C_{44} = 233$	$C_{11} = 167$ $C_{12} = 65$ $C_{44} = 80$	$C_{11} = 1079$ $C_{12} = 124$ $C_{44} = 578$

SiC is a very hard material. Taking Mohs hardness scale as an example, the value of talc is given by 1 and diamond is given by 10: SiC has the value of 9.3 [8].

SiC is chemically inert. For example, it is resistive to radiation and many chemicals. This is because the electron bonds between the silicon and carbon atoms inside SiC are extremely strong. More importantly, SiC has shown superior biocompatibility and is non-toxic in both *in vitro* and *in vivo* tests. In addition, SiC is multifunctional, originating from the possibility of adopting both silicon and carbon chemistry on its surface.

In conclusion, SiC is a material with exceptional physical properties (e.g. a low density, a high strength, a high thermal conductivity, high stability at high temperatures, a high resistance to shocks, low thermal expansion, a high refractive index, a wide but tunable bandgap) and chemical features. They present multiple options for smart devices through their electrical, chemical, and optical properties [5, 9–15].

1.1.2 SiC Applications

Thanks to its unique physical properties (e.g. electrical, thermal properties), SiC has found wide and varied applications where high blocking voltages or high switching frequencies are required [5, 9–15]. Shockley thus predicted in the 1950s that SiC would quickly replace Si. SiC-based power electronics can greatly reduce the power losses of electrical energy in most generators and distribution systems. The higher frequency,

smaller dimensions, reduced cooling requirements, and greater efficiency obtained with SiC power electronics will give more efficient systems in any application where AC-DC, DC-AC, or DC-DC conversion is required. One example application of SiC is for compact power supply units with extremely low losses, which also keep the power supply network free of electric smog (the unwanted interference frequencies resulting from the use of computers) [5, 15].

SiC is also suited for space-saving control units and for variable-speed drives, which are generally mounted directly on the mortars. For these applications, homoepitaxial SiC films are generally required. However, the typical growth rate for homoepitaxial SiC layers is 5–10 $\mu m\ h^{-1}$. Thus, the epitaxial growth of SiC layers is very time-consuming, making them very expensive for most devices. The long production time and high cost of these epitaxial SiC layers are thus the main obstacles to overcome, in order to make SiC power devices more available to market [5, 11, 15]. In contrast, the latest discovery of new forms of SiC (e.g. nanoporous structures, superlattices) has triggered the development of SiC electronics, and in particular thin-film technologies [11].

Bulk SiC has become a more important compound in materials science, such as a support for loading heterogeneous catalysts, for hard coating (e.g. for cutting), for implantable sensors, and for protein separation and micro-fluidic systems where a porous SiC film is needed. Especially in recent years there has been increased attention to employing SiC as a valuable material for biomedical applications and as a transducer for biosensors. This is because SiC has the advantages of its chemical, tribological, and electrical properties. In addition, it can easily be integrated on a chip into a system. For example, SiC has been employed as an active material for micro-device fabrication [13, 14]. In addition, SiC offers an ideal surface to grow graphene, another important material with superior physical, chemical and electrical properties [16].

1.1.3 Scope of this Chapter

Since the physical and mechanical properties of SiC films and their related nanostructures (e.g. particles, wires, pores, etc.) as well as their applications in the fields of electronics, power devices, and biomedical applications have been widely reviewed and discussed [5, 9–15], we focus in this chapter only on the growth, interfacial properties, and electrochemical applications of 3C-SiC. The growth of 3C-SiC using various chemical vapor deposition (CVD) techniques is summarized. After the description of the interfacial properties (e.g. surface morphology, surface chemistry, and electrochemical properties) of 3C-SiC, the electrochemical applications of 3C-SiC films in the fields of electrochemical and biochemical sensing, energy storage and conversion are highlighted. Finally, we close this chapter with concluding remarks as well as discussion about the future research directions of 3C-SiC.

1.2 Synthesis of Silicon Carbide

1.2.1 Acheson Process

SiC is traditionally produced through the so-called Acheson process, where an Acheson graphite electric resistance furnace is required. At very high temperatures (>2500°C), a solid-state reaction occurs between two precursors, namely silica sand and petroleum coke, leading to the formation of SiC [15]. Crystalline SiC synthesized by the Acheson

process features different polytypes and varies in its purity. The common impurities are nitrogen and aluminum. By altering the heating processes and/or the distances of the graphite resistor heat source of the Acheson furnace, colorless, transparent, or variously color SiC films have been synthesized [17]. These manufactured SiC films have large grain sizes and are invariably contaminated with oxygen. Such an Acheson process is still used for the production of polycrystalline SiC films, which are often known by the name carborundum. The as-obtained SiC ceramic is quite suitable for grinding and cutting applications, such as abrasive and cutting tools. However, the Acheson process requires excessive energy input during SiC synthesis, and the quality of the synthesized SiC is rather poor.

1.2.2 Physical Vapor Transport

Several alternative methods have since been developed for the synthesis of pure SiC films. Physical vapor transport (PVT) is the most popular and successful method for growing large single SiC crystals [18, 19]. As the first method of the sublimation technique (also known as the Lely method) [20], the synthesis of SiC with limited crystal sizes was carried out under argon ambient at about 2500°C in a graphite container. The formed SiC crystals (or Lely platelets) presented good quality (e.g. micropipe densities of 1–3 cm^{-2}, dislocation densities of 10^2–10^3 cm^{-2}). Unfortunately, this technique has several major shortcomings, such as uncontrollable nucleation rates and dendrite-like growth processes. Later, a modified PVT method (also called the modified-Lelly method or seed sublimation method) was proposed. Such a method controlled SiC growth and improved the limited adjustment of the gas phase composition between the concentrations of dopant species and the complements of C and Si [21]. The sources and the seeds of SiC were placed perfectly in close proximity to each other, where a gradient of temperatures was established. In such a way, the transport of the material vapor above the seeds became possible at a low argon pressure. The conventional PVT method was further refined through a gas pipe between the source and the crucible into the growth chamber (M-PVT setup) [22, 23]. By use of such a M-PVT setup, high-quality 4H- and 6H-SiC wafers have been grown, with diameters up to 100 mm. An additional gas pipe was used to introduce dopant gases and/or small amounts of C- and Si-bearing gases ($SiH_4 : H_2 = 1 : 10$, propane). Namely, the gas phase composition was further controlled. By use of such a modified M-PVT setup, 15R-SiC and 3C-SiC have been also synthesized [23].

1.2.3 Chemical Vapor Deposition

The CVD technique is another suitable and widely investigated method to produce SiC samples in various forms (e.g. thin films, powders, whiskers, and nanorods, etc.) [16, 24–57]. For example, amorphous SiC powders have been prepared by a CVD method, where SiH_4 and C_2H_2 acted as the precursors and nitrogen as the carrying gas [24, 25].

Atmospheric pressure chemical vapor deposition (APCVD) is one of the first CVD techniques developed to deposit SiC [25]. During deposition, a carbonization process is initially applied to a clean Si surface, followed by SiC growth using Si- and C-containing precursors [26–28]. SiC growth rates of up to several $\mu m\, h^{-1}$ have been achieved, with the potential to be doped into n- and p- type materials. An APCVD system is a relatively

simple and easy setup due to the incorporation of few temperature sensitive components. Both epitaxial and polycrystalline 3C-SiC films have been deposited by APCVD. It is particularly advantageous for SiC epitaxy, where higher temperatures (1300°C) are typically required for the growth of single crystals of SiC on Si substrates.

Low-pressure chemical vapor deposition (LPCVD) is the second CVD system utilized for the growth of SiC films. Although the growth rates of SiC films during LPCVD processes are much lower than those in APCVD processes, generally more substrates can be accommodated in LPCVD systems, especially when resistive heating is used. Due to the vacuum system involved for a LPCVD system, it has much lower chamber pressure in comparison with an APCVD system. Therefore, a LPCVD reactor allows the exploitation of more varieties of precursors, as well as reducing impurity incorporation in the deposited films. In short, the LPCVD process generates generally higher quality SiC films with much better uniformity across large substrate areas. By means of LPCVD techniques, epitaxial 3C-SiC films have been grown on Si wafers [29]. In recent years, LPCVD has actually become a leading technique for the growth of polycrystalline 3C-SiC films on various substrates including SiO_2 and Si_3N_4. Doping can also be achieved during LPCVD processes, conducted by simply adding dopants (e.g. 1,3-disilabutane, nitrogen, etc.) into the feed gases [30–35]. For example, controlled nitrogen doping has been demonstrated by adding nitrogen or NH_3 as the precursor into the feed gases. By varying the fractions of dichlorosilane and 1,3-disilabutane in the gas mixtures, the residual stress and strain gradient of polycrystalline SiC films has been tuned [36].

The third CVD technique applied for the synthesis of SiC films is metal organic chemical vapor deposition (MOCVD), which is especially useful for the growth of thick SiC films on sapphire (001) and silicon (111) substrates. Diethylmethylsilane (DEMS) containing both Si and C atoms was used as an individual precursor. No gas carrier or bubbler was thus applied. The films grown at low temperatures (850 and 900°C) on both substrates showed crystalline 3C-SiC in the (111) orientation [37].

Plasma enhanced chemical vapor deposition (PECVD) has been employed to deposit SiC films at low temperatures. Due to the use of low temperatures during PECVD processes, it is feasible to deposit SiC on a variety of materials (e.g. aluminum) that are not possible during APCVD and LPCVD processes. Commercially available PECVD systems can thus be utilized for processes that benefit from future mass production of SiC. The low deposition temperatures also confirm its potential suitability for related processing. To grow SiC by means of PECVD, gas precursors such as SiH_4 and CH_4 [38, 39] as well as liquid sources such as $C_6H1_8Si_2$ (hexamethyldisilane) [40] have been used. The as-deposited SiC films are amorphous, and thus post-deposition annealing is required for crystallization. Altering deposition parameters such as pressure and gas flow ratios resulted in the control of the stress in the deposited films during these PECVD processes [39]. Moreover, both doped and undoped SiC can be synthesized by PECVD [41–47]. We have employed microwave plasma chemical vapor deposition (MWCVD) techniques to grow three different kinds of 3C-SiC films, namely nanocrystalline, microcrystalline and epitaxial (001) 3C-SiC films [16]. Table 1.2 lists the depositional conditions we applied for the growth of these 3C-SiC films by means of MWCVD.

Figure 1.2 shows scanning electron microscopy (SEM) and atomic force microscopy (AFM) images of three 3C-SiC films [16]. The nanocrystalline 3C-SiC film possesses a crystal size smaller than 50 nm (Figure 1.2a). Its surface is relatively smooth and

Table 1.2 Depositional parameters for the MWCVD growth of three 3C-SiC films [16].

Film type	Microwave power (W)	Gas pressure (Torr)	T_s (°C)	TMS content (ppm)
Nanocrystalline	700	20	~800	290
Microcrystalline	1800	45	~700	290
Epitaxial	2200	55	~850	140

Source: Reprinted with permission from ACS publisher.

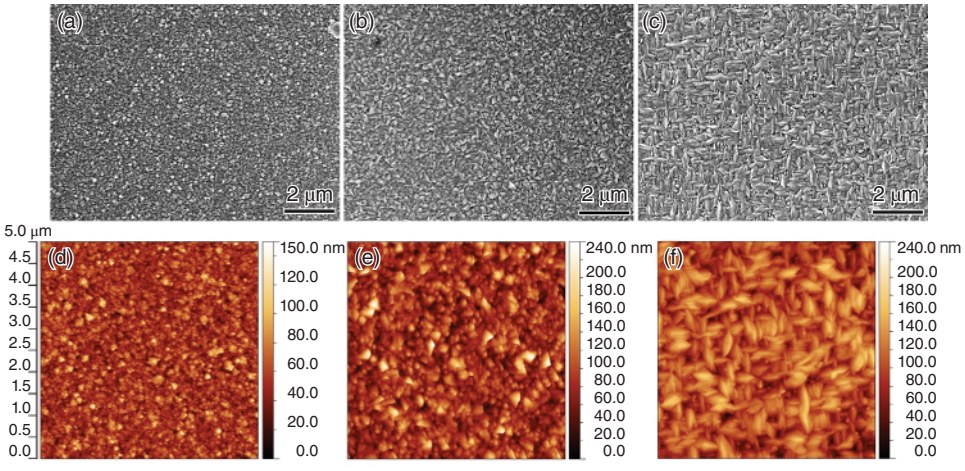

Figure 1.2 SEM (a–c) and AFM non-contact mode (d–f) images of a nanocrystalline (a, d), a microcrystalline (b, e), and an epitaxial (c, f) 3C-SiC film. The sizes of the AFM images are $5 \times 5\ \mu m^2$ [16]. Source: Reprinted with permission from ACS publisher, Copyright 2015.

has a root-mean-square (RMS) roughness of only 12.6 nm, as estimated from its AFM non-contact mode image shown in Figure 1.2d. The average crystal size of the microcrystalline 3C-SiC film is ~200 nm (Figure 1.2b). Its larger crystal size results in its higher surface roughness, which is measured to be 22.9 nm from the AFM image (Figure 1.2e). The SEM image of the epitaxial 3C-SiC film (Figure 1.2c) shows densely packed 3C-SiC crystals lying along the {110} directions of the Si wafer, presenting the very typical nature of heteroepitaxially grown 3C-SiC crystals on (001) Si [16, 48]. Its surface roughness is comparable to that of the microcrystalline 3C-SiC film, which is 20.6 nm determined by the AFM measurement (Figure 1.2f).

Remote microwave hydrogen plasma chemical vapor deposition (RPCVD) has been applied to grow amorphous hydrogenated SiC (a-SiC : H) films. Dimethylsilane (DMS) or tetramethylsilane (TMS) was used as a single-source precursor [49]. The Arrhenius plots of substrate temperature dependencies of the thickness-based film growth rate implied that the investigated RPCVD for DMS precursor is a non-thermally activated process, whereas for TMS precursor it is an adsorption-controlled one. An increase in the substrate temperature from 30 to 400°C caused the elimination of organic moieties from the films and the formation of SiC networks. These a-SiC : H films proved to be

useful as scratch-resistant protective coatings for optical glass elements and various metal surfaces [49].

Some other CVD techniques have been employed to grow 3C-SiC films. For example, the halide CVD process was applied to fabricate oriented stoichiometric 3C-SiC films in a rapid way. During such a process, the flow rates of precursors ($SiCl_4$ and CH_4) were controlled [54]. The (110)-oriented stoichiometric 3C-SiC films with lower densities of defects were obtained when the molar ratios of C precursor to Si precursor were in the range of 0.86–1.00. The maximum deposition rate was 883 μm h^{-1} when the molar ratio of C precursor to Si precursor reached 1.00, leading to a thickness of 1.7 mm in a deposition time of two hours. A twin plane propagation model has been proposed to explain the formation of ridge-like morphologies of SiC films. Another example, the low pressure hot-wall CVD technique, has been used for the growth of 3C-SiC films on Si (100) substrates [55]. The C/Si ratio played an important role in the crystalline quality and surface morphology of 3C-SiC films. Comparisons indicate that the optimal C/Si ratio for high crystalline quality of 3C-SiC films is 4.5. Noticeably, the polycrystalline grains of 3C-SiC films exhibited an epitaxial nature with irregular shapes and random distribution. Pyramid-like shapes and regular distribution were found along the {110} directions, dependent on the C/Si ratios. The changes in crystalline quality with increasing C/Si ratios were attributed to the competition of the formation of defects by excess carbon species with the etching of the atomic hydrogen. Meanwhile, the changes of surface morphology were due to the changes in secondary nucleation rates.

In past decades, more efforts have contributed to achieving homoepitaxial CVD growth of 3C-SiC films. Typically, it was done using silane (SiH_4) as the silicon precursor, and light hydrocarbons (e.g. ethylene or propane) as the carbon precursor. In some cases, only TMS was used as the precursor. Hydrogen gas, sometimes mixed with some argon, was used as carrier gas. The growth temperature and pressure were usually between 1500 and 1650°C and 100–1000 mbar, respectively. For example, the laser CVD technique has been applied for the epitaxial growth of 3C-SiC thin films on Si(001) substrates [50]. The epitaxial relationship was 3C-SiC(001){111}//Si(001){111} and multiple twins {111} planes were identified. The maximum deposition rate was 23.6 μm h^{-1}, which is about 5–200 times higher than that of conventional CVD methods. The density of twins increased with an increase in the thickness of 3C-SiC films. The cross-section of the films exhibited a columnar structure, containing twins at {111} planes that were angled at 15.8° to the surface of Si(001) substrates [50].

Conventional CVD equipment (c-CVD) was also employed for the growth of epi-SiC/Si-wafer/epi-SiC [51]. The Si wafer was double-side polished and mounted with a suspension mode in the c-CVD chamber. Homogeneous 3C-SiC (100) films were heteroepitaxially grown simultaneously on both surfaces of the suspended Si (100) wafer. Each film was uniform and continuous, with same trend of slight degradation from the inner to the outer region of the wafer. This technique offered a possible way to mass-produce high-quality 3C-SiC films on Si wafers in one run. The potential applications of 3C-SiC films (e.g. sensors, etc.) were thus also expanded.

Using PECVD techniques, the epitaxial deposition of 3C-SiC films has been achieved on (100) Si substrates [52]. A high density of defects (e.g. misfit dislocations, stacking faults, and twin boundaries) was generated in the film. Defect-induced strain distribution in the 3C-SiC film was analyzed by the geometric phase analysis method combined with X-ray diffraction (XRD) and Raman spectroscopy. The strain analysis at an atomic level revealed that periodic misfit dislocations at the interface generate high local

compressive strain (>20%) around the core of the dislocations in the SiC film, relaxing a major part of the intrinsic strain. A highly compressive interfacial layer was found to form between the SiC film and Si substrate, regardless of the carbonization temperature. This interfacial layer was linked with the carbonization step of the film growth process. In addition, twins and stacking faults provided a complementary route for strain relaxation during the film growth process. More strain was accommodated at the matrix/twin interface during twin nucleation rather than that at the growth stage.

The controlled growth of heteroepitaxial 3C-SiC films was achieved by use of a 915 MHz MWCVD reactor [53]. TMS and hydrogen were used as the resource gases. With an increase in MW power, the morphology of the SiC crystals evolved from randomly oriented nanocrystals to well-oriented pyramid-shaped crystals. Suggested from the rocking curves, the 3C-SiC film deposited at a MW power of 9 kW and a gas pressure of 50 mbar remained epitaxial in nature. An increase in TMS gas flow rates did not affect such an epitaxial feature. Uniform heteroepitaxial deposition of 3C-SiC film on 4-in. silicon wafer was then realized at a low deposition temperature (~860°C).

Various SiC nanostructures have been grown using CVD techniques [56, 57]. For example, the morphology control of one-dimensional (1D) SiC nanostructures was achieved by manipulating the composition of the catalysts (e.g. Fe_5Si_3, Fe_3Si) during MWCVD processes. Iron silicide was found to be the main catalyst to initiate the growth of 1D SiC nanostructures. As confirmed by high-resolution transmission electron microscopy (HRTEM), the stoichiometry of iron silicide governed the final morphology of 1D SiC nanowires (NWs). For the growth of SiC NWs, the catalyst is Fe_5Si_3, while it is Fe_3Si for the growth of SiC nanoneedles. A special orientation match between iron silicide catalyst and SiC NWs was observed during the growth of 1D SiC nanostructures, due to different etching resistivities of the catalyst particles under H_2 plasma [56]. Direct synthesis of ordered 3C-SiC nanosheet arrays has been also realized in a MWCVD reactor through utilizing planar defects formed during hetero-epitaxial growth of crystals with close-packed lattices [57]. TMS was used as a single source precursor and diluted in hydrogen gas. The plasma with a high MW power (e.g. 2500 W) was applied to activate the gas phase reaction. With a very low concentration of TMS (e.g. 140 ppm), the growth of the 3C-SiC epitaxial layer was achieved at a low growth rate (~50 nm h^{-1}). The grown 3C-SiC nanosheet arrays are well oriented on (001) and (111) Si substrates. The planar defects and the plasma environment were identified as key factors to determine the resulting 2D nanosheet arrays. Consequently, a "planar defect induced selective growth" effect was proposed to elucidate the corresponding growth mechanism [57].

In summary, various 3C-SiC films and nanostructures have been grown at different sizes (>3 in.) by altering CVD techniques, substrates, and growth parameters (e.g. power density, gas pressure, type and concentration of precursors, and growth temperature, etc.).

1.3 Properties of Cubic Silicon Carbide

1.3.1 Surface Morphology

From further analysis of growth conditions summarized in Table 1.2, one can see that the changes in morphology of three 3C-SiC films are possible by controlling the MW

powers, gas pressures, and the concentrations of TMS precursors during MWCVD deposition [52]. For example, at low MW powers and high TMS concentrations, nanocrystalline 3C-SiC films are grown. This is because of high secondary nucleation rates under these conditions. An increase in the MW power enhances the concentration of atomic hydrogen, which is an important species in determining the crystallinity of a 3C-SiC film during MWCVD deposition [52, 58]. It removes the defects and amorphous phase in a 3C-SiC film through a continuous etching process [52, 58]. The higher the concentration of atomic hydrogen, the stronger the etching will be. Since the defects and amorphous phase can serve as sites for secondary nucleation, their effective removal will improve in turn the crystallinity of the 3C-SiC films [52, 58]. As a result, microcrystalline 3C-SiC films with larger crystal sizes and higher crystal quality are formed at high MW powers. Further increase in MW power or reduction of TMS concentrations led to the epitaxial growth of 3C-SiC films on the (001) Si wafer [52].

More detailed information about the composition of nanocrystalline, microcrystalline, and epitaxial 3C-SiC films has been revealed by XRD measurements. Peaks positioning at 35.6°, 41.4°, 60.0°, and 90.0° are indexed to the (111), (200), (220), and (400) reflexes of 3C-SiC, respectively. However, certain differences are observable. For both nanocrystalline and microcrystalline 3C-SiC films, strong (111) reflex exists. Weak (220) reflex is only observed for the microcrystalline 3C-SiC film: an indication of its polycrystalline nature. The intensity of the (220) reflex is much weaker in the nanocrystalline 3C-SiC film. For the epitaxial 3C-SiC film, only (200) and (400) reflexes are present, indicating its perfect (001) orientation [16].

Except for the 3C-SiC crystals, it is well understood that amorphous phases normally form at the grain boundaries during the CVD growth of 3C-SiC films [52]. Such information for these three 3C-SiC films was confirmed using micro-Raman measurements [16]. For all 3C-SiC films, the characteristic Raman peak at ~800 cm^{-1} is observable, corresponding to the transverse optical (TO) phonon of SiC. The full width at half maximum (FWHM) of this SiC TO peak for nanocrystalline, microcrystalline, and epitaxial 3C-SiC films is >40, 17, and 24 cm^{-1}, respectively. In comparison with that for a nanocrystalline 3C-SiC film, the SiC TO peaks for both microcrystalline and epitaxial 3C-SiC films are sharper, indicating their better crystallinity. In addition to the SiC TO band, peaks corresponding to the existence of an amorphous carbon phase are also observable at ~1320 cm^{-1} (D band) and ~1600 cm^{-1} (G band) for both nanocrystalline and microcrystalline 3C-SiC films. Nevertheless, since the Raman efficiency of SiC is only a tenth of that of the amorphous carbon [59], the strong D and G bands do not imply an extremely large amount of amorphous carbon phase in the 3C-SiC films. A broad peak positioning at ~900 cm^{-1} is attributed to the Si-C rocking in Si-CH_3 [60–63]. The existence of the C-H bonding has been further confirmed by the secondary ion mass spectrometry (SIMS) measurements [64]. Such an observation indicates the presence of the amorphous SiC phase in both 3C-SiC films [60–63]. However, these three peaks completely disappear in the epitaxial 3C-SiC film. This result indicates strongly that no amorphous phase is incorporated into the epitaxial 3C-SiC film. In other words, the epitaxial 3C-SiC film is composed solely of 3C-SiC crystal. Furthermore, a shift in the position of this SiC TO peak is observed. For the microcrystalline and nanocrystalline 3C-SiC films, it shifts to lower wavenumbers in comparison with that of the epitaxial 3C-SiC film, indicating reduced crystallinity for both microcrystalline and nanocrystalline 3C-SiC films. However, a slight upshift

of this SiC TO peak for a nanocrystalline SiC film in comparison with that of a microcrystalline SiC film is reasonable. This is because the nanocrystalline 3C-SiC film contains more amorphous phase, whose thermal expansion coefficient is different from that of a microcrystalline 3C-SiC film. Moreover, the thickness of the nanocrystalline 3C-SiC film is different from that of the microcrystalline 3C-SiC film. These factors lead to the different stress levels in the nanocrystalline 3C-SiC film, resulting in the upshift of its Raman peak in comparison with that of the microcrystalline 3C-SiC film.

To get deep insight into the microscopic structures of nanocrystalline, microcrystalline, and epitaxial 3C-SiC films, their transmission electron microscopy (TEM) images were recorded. As shown in Figure 1.3, the difference in crystal sizes of these 3C-SiC films is clearly seen even from their low magnification TEM images. For the nanocrystalline 3C-SiC film, two kinds of crystals are present but with significant difference in their sizes, as indicated in Figure 1.3a with arrows. The small crystals are about ~5 nm in size, whereas the large ones are tens of nanometers in size. They were confirmed to be 3C-SiC crystals by HRTEM measurements. As shown in Figure 1.3d, the typical lattice fringes of these 3C-SiC crystals feature an interplanar spacing of 0.252 nm for their {111} planes. Moreover, a certain amount of planar defects (twins and stacking faults) is found in these crystals. Those twins and stacking faults lie parallel to the {111} planes, as denoted by the circles in Figure 1.3d. Regardless of their higher crystallinity,

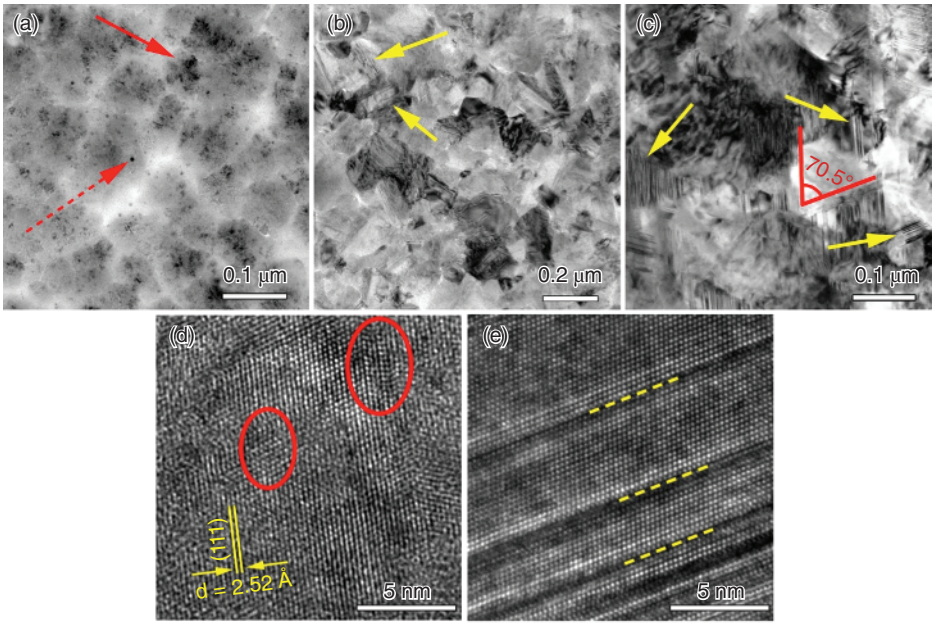

Figure 1.3 Low magnification TEM images of a nanocrystalline (a), a microcrystalline (b), and an epitaxial (c) 3C-SiC film; HRTEM images of one typical 3C-SiC crystal in the nanocrystalline (d) and microcrystalline (e) 3C-SiC film. The arrows in (a) indicate the 3C-SiC crystals with different sizes in the nanocrystalline 3C-SiC film. The arrows in (b) and (c) indicate the existence of planar defects in the microcrystalline and epitaxial 3C-SiC films. The circles in (d) denote the existence of planar defects, of which positions are indicated with dashed lines in (e) [16]. Source: Reprinted with permission from ACS publisher, Copyright 2015.

planar defects (arrows) are also observed in the microcrystalline (Figure 1.3b) and epitaxial (Figure 1.3c) 3C-SiC films. Figure 1.3e shows the HRTEM image of one typical 3C-SiC microcrystal with planar defects indicated by the dashed lines. The formation of planar defects is difficult to avoid. It is a very common phenomenon during the growth of various SiC structures [56, 64]. This is because the formation energies of these planar defects are low. During MWCVD processes, the energy generated by the mismatches (e.g. lattice mismatch, thermal expansion coefficient mismatch, etc.) between the SiC film and the substrate is sufficient to trigger the formation of these phase defects, leading to their high concentration in the crystals. Even though the existence of the planar defects is clearly observable throughout the whole film, no small angle grain boundaries exist in the epitaxial 3C-SiC film. This indicates such an epitaxial 3C-SiC film can be viewed as a single 3C-SiC crystal but with a high density of planar defects. This result is in good accordance with the Raman observation, where the epitaxial 3C-SiC film is found to be composed solely of the 3C-SiC crystal without any amorphous phase.

Therefore, there are significant differences in the compositions of the nanocrystalline, microcrystalline, and epitaxial 3C-SiC films. Both nanocrystalline and microcrystalline 3C-SiC films consist of amorphous carbon, amorphous SiC, and 3C-SiC crystals, while the epitaxial 3C-SiC film is composed solely of 3C-SiC crystals. Moreover, there are big differences in the crystal sizes of the nanocrystalline and microcrystalline 3C-SiC films. Furthermore, both nanocrystalline and microcrystalline 3C-SiC films are polycrystalline, while the epitaxial 3C-SiC film shows perfect (001) orientation. In addition, a large number of planar defects are incorporated in the 3C-SiC crystals for the nanocrystalline, microcrystalline, and epitaxial 3C-SiC films [16].

1.3.2 Electrochemical Properties

Understanding the mechanisms of charge transfer across the interfaces of various SiC films and the electrolytes is of importance and significance. It is a basic prerequisite for exploring the practical applications of these SiC films [65].

SiC has been tried more than 70 years ago as an electrode. Single crystalline SiC film behaved in a similar way to a noble electrode [66]. Single SiC films were used to construct impedance and temperature sensors. SiC based biomedical needles were used for open-heart surgery monitoring and graft monitoring of organs during transportation and transplantation [67]. However, it was troublesome to get the right contacts due to low conductivities of these films. Later, the nanocrystalline 3C-SiC film was found to exhibit much higher electron mobility than a single crystalline SiC film [68, 69]. It was thus employed as a novel electrode material for electrochemical applications (e.g. for electrochemical sensing applications) [55, 70]. Moreover, the properties of 3C-SiC films, especially their electrochemical properties, were found to be tunable through controlling the microstructures of 3C-SiC films (e.g. crystallinity, crystal sizes, defects, and composition, etc.) [16]. For example, by manipulating the deposition conditions (e.g. power density, growth temperature, etc.) during MWCVD processes, the nanocrystalline, microcrystalline, and epitaxial (001) 3C-SiC films have been grown with altered electrochemical properties [16].

First, these 3C-SiC films exhibited different electrical conductivities, as measured by a four-point-probe technique. Both nanocrystalline and microcrystalline 3C-SiC films possess a sheet resistance of $\sim 3300\,\Omega\,cm^{-2}$, whereas the epitaxial 3C-SiC film only

shows a sheet resistance of 86 $\Omega\,cm^{-2}$. Their conductivities result from the existence of defects in the 3C-SiC films (e.g. planar defects, grain boundaries, and the amorphous phases). The average oxygen concentration of the nanocrystalline 3C-SiC film was enhanced, and then the oxygen accumulated at crystal defects, resulting in much better conductivity [68, 69]. According to experimental investigation [71] and theoretical simulation [72], the planar defects in 3C-SiC films have high electrical conductivities, which are even higher than those of heavily nitrogen doped ($5 \times 10^{18}\,cm^{-3}$) 3C-SiC films. In contrast, the amorphous phases show low electrical activities [73, 74]. Even though the nanocrystalline and microcrystalline 3C-SiC films contain significant amounts of planar defects, the existence of amorphous phases at the grain boundaries might resist the passage of the electric current between the SiC crystals, resulting in increased resistivity. For the epitaxial 3C-SiC film, it is free of the amorphous phases. In addition, anti-phase boundaries normally exist at the boundaries between the (001)-oriented SiC crystals, which give a further rise in its electrical conductivity, making the film even metallically conductive [75]. In this context, the epitaxial 3C-SiC film presents a higher electrical conductivity in comparison with the nanocrystalline and microcrystalline 3C-SiC films. Note that those 3C-SiC films were undoped. However, according to the values of their electrical conductivities, these 3C-SiC films could be applied as electrodes.

Prior to examining electrochemical properties of the nanocrystalline, microcrystalline, and epitaxial (001) 3C-SiC films, they were carefully cleaned to remove inorganic and organic contamination. After that, the films were treated in a hydrofluoric acid (HF) solution, resulting in OH-terminated surfaces [76, 77]. The double layer capacitive behavior of these 3C-SiC films was investigated using cyclic voltammetry in both aqueous (0.1 M H_2SO_4) and non-aqueous (0.1 M tetrabutylammonium tetrafluoroborate in acetonitrile) solutions (Figure 1.4). The calculated double layer capacitances of the epitaxial 3C-SiC film were 6.3 and 5.2 $\mu F\,cm^{-2}$ in aqueous and non-aqueous solutions, respectively. Higher capacitances of 14.2 $\mu F\,cm^{-2}$ in the aqueous solution and 10.9 $\mu F\,cm^{-2}$ in the non-aqueous solution were obtained for the microcrystalline 3C-SiC film. Taking into consideration the surface roughness of a microcrystalline

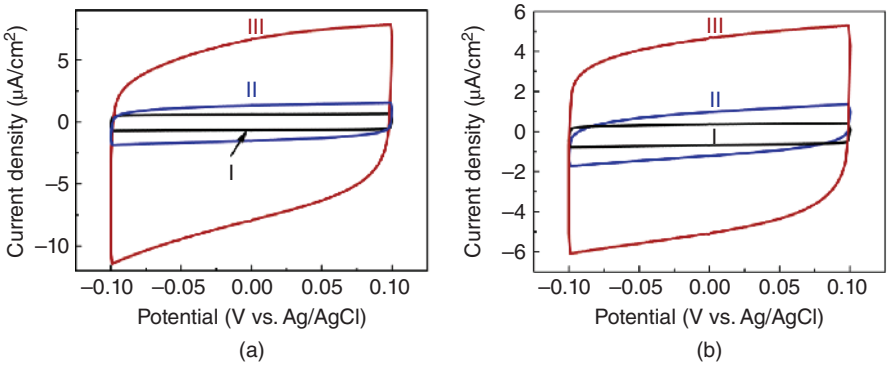

Figure 1.4 Cyclic voltammograms of an epitaxial (I), a microcrystalline (II), and a nanocrystalline (III) 3C-SiC film at a scan rate of 100 mV s^{-1} in 0.1 M H_2SO_4 (a) and in 0.1 M tetrabutylammonium tetrafluoroborate dissolved in acetonitrile (b). The currents were normalized with the geometric areas of the 3C-SiC films [16]. Source: Reprinted with permission from ACS publisher, Copyright 2015.

3C-SiC film, its specific capacitances were double those of an epitaxial 3C-SiC film. The nanocrystalline 3C-SiC film possessed the highest double layer capacitances (e.g. 72.7 μF cm^{-2} in aqueous solutions and 48.5 μF cm^{-2} in non-aqueous solutions, respectively). Once the real surface area of this nanocrystalline 3C-SiC film was taken into account, the corresponding capacitances were 56.8 and 37.9 μF cm^{-2}, respectively. Depending upon MWCVD deposition conditions for the nanocrystalline 3C-SiC films, their double layer capacitances varied in the range from ~40 to ~100 μF cm^{-2}. In contrast to the nanocrystalline 3C-SiC film, the double layer capacitances of the microcrystalline and epitaxial 3C-SiC films exhibited much narrower distributions [16].

The electrochemical activity of the nanocrystalline, microcrystalline, and epitaxial (001) 3C-SiC films was examined in water-soluble redox probe (e.g. $[Fe(CN)_6]^{3-/4-}$, $[Ru(NH_3)_6]^{2+/3+}$) contained aqueous solutions as well as in organic solvent-soluble redox probes (e.g. ferrocene and quinone) contained non-aqueous solutions [78]. Figure 1.5 shows cyclic voltammograms of four redox probes on the nanocrystalline 3C-SiC film. Well-defined redox waves are seen for all cases. The values of ΔE_p (the difference of the anodic peak potential from the cathodic peak potential) and I_p^{ox}/I_p^{red} (the ratio of the anodic peak current, I_p^{ox}, to the cathodic peak current, I_p^{red}) are 130 mV, 1.0 for $Ru(NH_3)_6^{2+/3+}$ redox couple (Figure 1.5a); 120 mV, 1.0 for $Fe(CN)_6^{3-/4-}$ redox couple (Figure 1.5b); 150 mV, 1.0 for quinone (Figure 1.5c); and 140 mV, 1.0 for ferrocene (Figure 1.5d), respectively. Both I_p^{ox} and I_p^{red} are proportional to the square roots of scan rates from 10–200 mV s^{-1}. These results indicate that on the nanocrystalline 3C-SiC film these four faradaic reactions are quasi-reversible and controlled by the diffusion of those redox probes. Consequently, the nanocrystalline 3C-SiC film can be applied as a novel electrode material.

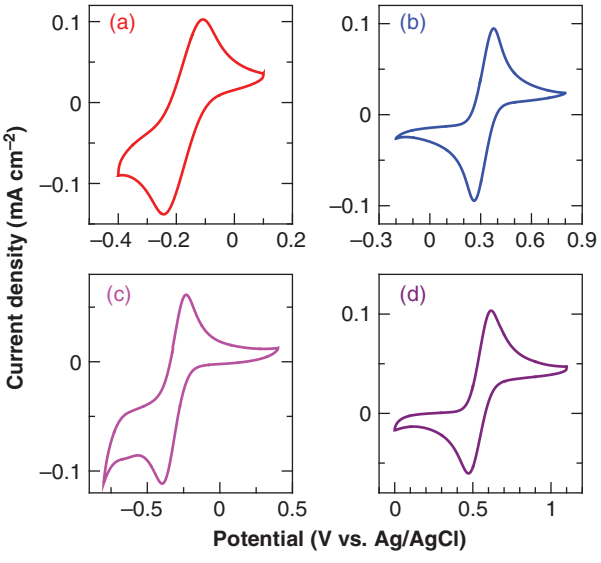

Figure 1.5 Cyclic voltammograms of a nanocrystalline 3C-SiC film at a scan rate of 10 mV s^{-1} in 1.0 mM $Ru(NH_3)_6^{2+/3+}$ (a) and 1.0 mM $Fe(CN)_6^{3-/4-}$ dissolved in 0.1 M KCl solution (b), as well as in 1.0 mM quinone (c) and 1.0 mM ferrocene (d) dissolved in 0.1 tetrabutylammonium tetrafluoroborate solution [78] Source: Reprinted with permission from Wiley. Copyright 2012.

For the microcrystalline and epitaxial (001) 3C-SiC films, well-defined redox waves are also observed in water-soluble redox probes (e.g. $[Fe(CN)_6]^{3-/4-}$, $[Ru(NH_3)_6]^{2+/3+}$) containing aqueous solutions as well as in organic-solvent soluble redox probes (e.g. ferrocene and quinone) containing non-aqueous solutions [78]. The peak currents are proportional to the square roots of scan rates, indicating that the faradaic reactions of those redox probes are controlled by their diffusion. Moreover, the reversibility of the redox probes on all 3C-SiC films in aqueous solutions is better than that in the non-aqueous solutions, judging from their values of ΔE_p and $E_p - E_{p/2}$ (the difference of anodic/cathodic peak from its half-peak potential). Further comparison of ΔE_p and $E_p - E_{p/2}$ for the same redox probe on different 3C-SiC films leads to the conclusion that the best reversibility of redox probes is on the epitaxial 3C-SiC film, and the worst reversibility of redox probes is on the nanocrystalline 3C-SiC film. The difference in the reversibility of the redox probes originates from different charge transfer resistances of these 3C-SiC films. For example, the lowest charge transfer resistance is about 580 Ω for the epitaxial 3C-SiC film and the highest value is about 3300 Ω for the nanocrystalline 3C-SiC film [16]. In conclusion, the measurements of four different redox probes featuring varied electrode kinetics (e.g. the appearance of redox waves in different potential ranges) on three 3C-SiC films suggest that three 3C-SiC films can be applied in different media as well as in different potential ranges. However, the epitaxial 3C-SiC film presents the lowest double-layer capacitance and the highest reversibility of redox probes, because of its perfect (001) orientation and high phase purity. The highest double-layer capacitance and the lowest reversibility of redox probes have been realized on the nanocrystalline 3C-SiC film, due to its concentration of grain boundaries, amorphous phases, and high diversity in crystal sizes.

The electrochemical potential window of a nanocrystalline 3C-SiC film was further measured in an aqueous solution (0.1 M H_2SO_4). The obtained cyclic voltammogram was featureless in the scanned potential range [70], indicating that the SiC/electrolyte interface is almost polarizable. The currents were stable with repeated sweeps and independent of the composition and pH value of the electrolytes. As shown in Figure 1.6, the capacitive current of the nanocrystalline 3C-SiC film is about 3–5 times smaller than that of a glassy carbon electrode, but 20–50 times larger than that of a boron-doped diamond electrode. Here, the boron concentration of this boron-doped diamond

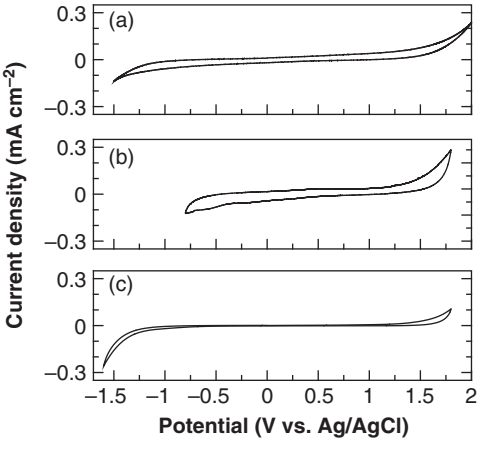

Figure 1.6 Cyclic voltammograms of a nanocrystalline 3C-SiC film (a), a glassy carbon electrode (b), and a boron-doped diamond electrode (c) in 0.1 M H_2SO_4 at a scan rate of 100 mV s^{-1}. The boron concentration of the boron-doped diamond electrode is 5×10^{20} cm^{-3} [70]. Source: Reprinted with permission from from ACS. Copyright 2011.

electrode is 5×10^{20} cm^{-3}. Moreover, the increase in anodic current on this heavily boron-doped diamond electrode is much faster than that on the nanocrystalline 3C-SiC film when the potential is higher than 1.2 V. The decrease in cathodic current on this heavily boron-doped diamond electrode is much faster than that on the nanocrystalline 3C-SiC film. Defined by a current density of 0.1 mA cm^{-2} as the threshold, the deduced potential window for a nanocrystalline 3C-SiC film SiC is about 3.0 V, which is slightly narrower than that of the boron-doped diamond electrode (3.2 V), but much wider than that of a glassy carbon electrode (2.2 V).

Fundamental electrochemical studies on n-type 6H-SiC and 4H-SiC electrodes have also studied the ferri-/ferrocyanide redox couple contained aqueous electrolytes [79]. To determine the energetic positions of the SiC band edges, as well as to investigate the electron-transfer kinetics between SiC and the ferricyanide molecules, cyclic voltammetry and impedance spectroscopy measurements were performed over a wide potential range. For both n-type 6H-SiC and 4H-SiC electrodes, a broad distribution of surface states with energy levels close to the conduction band was found to mediate electron transfer. This results in deviations of the observed charge transport characteristics from the predictions of well-established models. Detailed evaluation of the impedance data clarified further the correlation of the charge-transfer resistances of ferricyanide reduction reactions with the potential-dependent distribution of surface states [79]. The stability of n-type 6H-SiC photoelectrodes in buffered aqueous electrolytes was also investigated using cyclic voltammetry [80]. In pure Tris buffer, photogenerated holes accumulated at the interface under anodic polarization, resulting in the formation of a porous surface oxide layer. To significantly enhance the stability of the SiC photoelectrodes, two possibilities were then proposed. As the first approach, redox molecules were added to the buffer solution and then hole transfer to these molecules was kinetically facilitated. The second approach was to induce water oxidation through depositing a cobalt phosphate catalyst on the SiC surface. AFM and X-ray photoelectron spectroscopy (XPS) measurements confirmed that both approaches effectively suppressed photocorrosion of the SiC electrodes [80]. Furthermore, surface polishing of n-type polycrystalline 3C-SiC film was achieved by means of electrochemical etching, conducted in diluted HF solution under constant applied current density. No UV illumination was applied [81]. Such electropolishing led to a smooth 3C-SiC surface, which was flat and featureless. There was no sign of intergranular corrosion or other degradation phenomena related to the polycrystalline structure. After optimizing etching conditions (e.g. HF concentration, current density, and etching time), the roughness of this polycrystalline 3C-SiC film was reduced by more than half compared with its initial value [81].

1.3.3 Surface Chemistry

To expand the applications of SiC films, especially their electrochemical and biochemical applications, the surfaces of SiC films have been decorated with various terminations and/or organic molecules [82–88].

1.3.3.1 Surface Terminations

Since SiC possesses both silicon and carbon atoms, SiC films have different surface terminations. For example, cleaning (001) 3C-SiC films using HF as an oxide removal

agent yielded Si-OH and C-H terminated surfaces [89]. Hydrogen passivation of SiC surfaces by high-temperature hydrogen annealing has been theoretically discussed [90]. Hydrogenated hexagonal SiC {0001} surfaces offer the interesting possibility of gaining insight into the formation of silicon- and carbon-rich reconstructions. This is due to the fact that, to date, hydrogenation is the only method of providing oxygen-free surfaces with a C to Si ratio of 1 : 1. The electronic properties of hydrogen-free SiC {0001} surfaces are eluded. SiC {0001} surfaces are the only known semiconductor surfaces that can be prepared in their unreconstructed (1×1) state with one dangling bond per unit cell by photon-induced hydrogen desorption. These surfaces give indications of a Mott-Hubbard surface band structure. Hydrogenation of 6H-SiC was also achieved experimentally by high-temperature hydrogen treatment [91]. Hydrogenation was confirmed by the observation of sharp Si-H stretching modes on SiC(0001). The surfaces showed no sign of surface oxide in XPS even after two days in air. The treated surfaces showed a low-energy electron diffraction pattern, representative of unreconstructed surfaces of extremely high crystallographic order. The absence of surface bending for n- and p-type SiC films is indicative of electronically passivated surfaces with densities of charged surface states in the gap of below 7×10^{10} and 1.7×10^{12} cm^{-2} for p- and for n-type SiC films, respectively [91].

A plasma-based method has been utilized to yield chlorine-terminated SiC surfaces [92]. During such a process, the surface roughness of 6H-SiC film was not affected. A significant reduction in oxygen and a corresponding rise of chlorine core level intensities were found in the XPS results. These indicated halogen termination. Contact potential difference and surface photovoltage measurements showed the formation of negative surface dipoles and approximately flat band surface potentials after chlorine termination of (0001) n-type 6H-SiC [92].

1.3.3.2 Surface Functionalization

Due to the existence of Si and C phases, both silicone and carbon chemistry have been utilized for surface functionalization of various SiC films and nanostructures. Figure 1.7 summarizes some reported functionalization strategies.

A 3C-SiC surface has been thermally functionalized with 3-aminopropyl triethoxysilane (APTES). In a sealed chamber, the SiC surface was coated with 200 µl APTES.

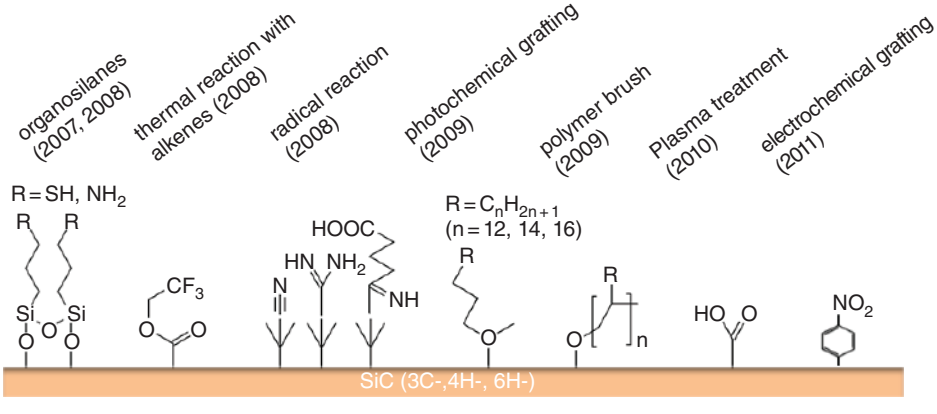

Figure 1.7 Reported strategies for surface functionalization of various SiC films and nanostructures.

The chamber was then heated up to 60°C for 10 minutes at 6 mbar and then further increased to 150°C for 1 hour. Prior to such functionalization, SiC substrates were cleaned in 50% HF solution with the intention of removing the native oxide on the SiC surface. Meanwhile the hydroxyl-terminated surface was obtained. The XPS of functionalized SiC films showed a prominent peak positioned at about 400 eV. This approach was also conducted on SiC epi-layers. Thermal grafting of both alkylated and fluorine-containing 1-alkynes and 1-alkenes onto SiC has been realized [93]. XPS, infrared reflection–absorption spectroscopy (IRRAS), and near-edge X-ray absorption fine structure (NEXAFS) spectroscopy measurements indicated that acetyl groups were presented at the organic–inorganic interfaces of alkyne-modified SiC surfaces. The static water contact angles measured on these interfaces were up to 120°. Using AFM, the tribological properties of these organic monolayers were also explored. The fluorinated monolayers exhibited significant reduction of adhesion forces, friction forces, and wear resistance compared with non-fluorinated molecular coatings, and especially bare SiC substrates. The successful combination of hydrophobicity and excellent tribological properties makes these strongly bound, fluorinated monolayers promising candidates for applications in high-performance microelectronic devices [93].

The wet-chemical functionalization of n-type (100) and (111)3C-SiC surfaces has been demonstrated with self-assembled monolayers (SAMs) of aminopropyldiethoxymethylsilane (APDEMS) and octadecyltrimethoxysilane (ODTMS) [94]. These organic layers were found to be smooth and densely packed on 3C-SiC surfaces. Confirmed from combined contact potential difference and surface photovoltage measurements, the heterostructure functionality and surface potential of these SAMs were found to be tunable once different organosilane precursors were utilized. Molecular dipoles significantly affected the work functions of the modified surfaces. The magnitude of the surface band bending was reduced on the hydroxylated surfaces with organosilanes, indicating that partial passivation of electrically active surface states is achieved. Self-assembly of APDEMS and ODTMS onto 6H-SiC films was also demonstrated [83]. The structural and chemical properties of these layers were studied by contact angle measurements, AFM, thermal desorption, and XPS. The organic layers were smooth and the wetting angles were up to 100°. Desorption temperatures in the range of 557°C proved the covalent bonding of the organic silane molecules to the SiC surface. The monolayers of 11-hydroxyundecyphosphonic acid and 9,10-diphenyl-2,6-diphosphonoanthracene have been self-assembled on 6H-SiC films [95]. Structural and chemical properties of these monolayers were investigated through contact angle measurements, AFM, XPS, and Fourier transformation infrared (FTIR) spectroscopy. Covalent bonding of the phosphates to both (0001)- and (000-1)-oriented 6H-SiC crystal faces was confirmed. Electrical characterization was achieved through contact potential difference and surface photovoltage measurements, which revealed significant changes in the work functions of the substrates by monolayer formation.

A short chain molecule of allylamine has been photochemically attached to 3C-SiC films, as confirmed by SIMS and XPS measurements [96]. The maximum coverage of allylamine on a 3C-SiC surface was achieved after four hours of UV illumination. With further UV illumination, allylamine cross-polymerized slightly with each other. The allylamine dense monolayer was formed under UV illumination for four

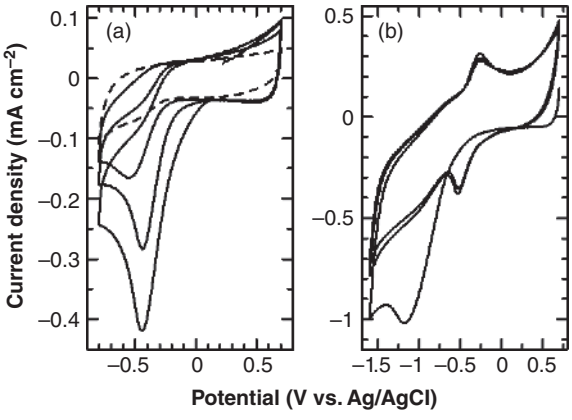

Figure 1.8 (a) Electrochemical grafting of a nanocrystalline 3C-SiC film with 1.0 mM 4-nitrobenzene diazonium tetrafluoroborate using cyclic voltammetry. The electrolyte was 0.1 M tetrabutylammonium tetrafluoroborate in acetonitrile. The scan rate is 200 mV s^{-1}. (b) Electrochemical reduction of nitrophenyl film in 1 M KCl in a mixture of ethanol : water (V : V = 1 : 9) at a scan rate of 100 mV s^{-1} [70]. Source: Reprinted with permission from ACS publisher, Copyright 2011.

hours. From its XPS results, the maximum surface density was calculated to be $\sim 4 \times 10^{14}$ molecules cm^{-2}.

The nanocrystalline 3C-SiC film has been modified using an electrochemical approach, namely by means of electrochemical reduction of diazonium salts [70]. The attachment was confirmed by electrochemical, time-of-flight secondary ion mass spectrometry (ToF-SIMS), and XPS measurements. Figure 1.8a shows voltammograms for the reduction of 4-nitrobenzene diazonium salt on a nanocrystalline 3C-SiC film. An irreversible reduction peak centered around -440 ± 60 mV (vs. Ag/AgCl) is detected during the first cycle. The cathodic peak potential shifts toward more negative potentials in subsequent cycles. The peak disappears after more than 10 cycles (dashed line). The peak arises by the reduction of diazonium salt cations, yielding radical species that covalently bind to the SiC surface. The decreased cathodic peak current and the negative shift of the cathodic peak potential indicate the formation of an insulating film, where either the reduction is halted or the electron transfer through the formed film is kinetically slowed down as a function of time [97–99]. Moreover, the redox currents of $Fe(CN)_6^{3-/4-}$ on a nitrophenyl layer functionalized SiC surface was strongly suppressed. As shown in Figure 1.8b, such a functionalized surface exhibited in the first cycle a large irreversible reduction peak at -1.10 ± 0.05 V (vs. Ag/AgCl) in the aqueous solution of ethanol : water (V : V = 1 : 9). This is due to the electrochemical reduction of nitrophenyl (Ar-NO_2) groups to amine (Ar-NH_2) or hydroxyaminophenyl (Ar-NHOH) groups [97–99]. In the second and subsequent cycles, this reduction peak was drastically diminished, indicating that nearly all electroactive nitrophenyl groups are reduced in the first scan. The reversible couple at $E_{1/2} = -350 \pm 30$ mV (vs. Ag/AgCl) appeared only after the first cycle, indicating an incomplete reduction process of -Ar-NO_2 to -Ar-NH_2 [97–99]. The density of nitrophenyl on the SiC surface, evaluated from the charge transferred for the wave at -1.10 V (vs. Ag/AgCl), was 3.1×10^{15} cm^{-2} or 5.1×10^{-9} mol cm^{-2}. In SIMS, nitrogen-related characteristic peaks (CN^-, CNO^-, NO_2^-, $C_6H_4NO_2^-$, and -$OC_6H_4NO_2^-$) are clearly seen in the functionalized areas. The XPS of a nitrophenyl-grafted SiC surface did present a broad N peak where two sharp peaks at 399 and 406 eV were simulated [100], assigned to the NO_2 group and some reduced nitrogen-containing functionalities, respectively.

1.4 Electrochemical Applications of Cubic Silicon Carbide Films

3C-SiC films feature wide potential windows, stable capacitance currents, and good electrochemical response toward electroactive species. Therefore, they have been employed as the electrode materials for various electrochemical applications.

1.4.1 Electrochemical Sensors

3C-SiC thin films have been used to construct electrochemical sensors. As an environmentally friendly and alternative electrode material, nanocrystalline 3C-SiC film has been employed as an electrode for anodic stripping voltammetric detection of trace metal ions [101]. The obtained detection limits for Cu^{2+} and Ag^{+} ions were as low as 6 and 4 ppb, respectively. In addition to the individual detection of these metal ions, the 3C-SiC electrode also showed good capability and good reproducibility for simultaneous detection of Cu^{2+} and Ag^{+} ions [101].

An electrochemical dopamine sensor was fabricated using epitaxial 3C-SiC film [16]. This is because epitaxial 3C-SiC film shows a lower background current and better reversibility for the redox probes in aqueous solutions than a nanocrystalline SiC film [16]. In pH 7.4 phosphate buffer solution containing 100 μM dopamine, a well-defined oxidation peak appeared at 0.4 V. A small reduction peak was observable at ~0 V. An increase in the scan rates led to the proportional enhancement of the anodic peak current densities. These results implied that irreversible oxidation of dopamine on the epitaxial 3C-SiC film is a diffusion-controlled process, instead of an adsorption-controlled one. Differential pulse voltammetry was adopted for the monitoring of dopamine. The anodic peak current density was linearly enhanced with the concentration of dopamine in the concentration range of 2–200 μM. The detection limit was determined to be 0.7 μM or 0.1 mg l^{-1} [16]. Although the limit-of-detection of dopamine on the epitaxial 3C-SiC film was not as low as that obtained on other electrodes reported in the literature [102], the workable concentration range for dopamine detection on the epitaxial 3C-SiC film was still one to two orders lower than its concentration in tissue (4–10 mg l^{-1}) [103, 104]. Therefore, the epitaxial 3C-SiC film is a suitable and promising electrode material for electrochemical determination of dopamine.

1.4.2 Biosensors

Surface functionalized SiC films have been applied for biochemical applications. For example, by utilizing self-assembled layers with functional terminal groups, immobilization of proteins was demonstrated [83, 94, 95]. The bio-application of a nanocrystalline 3C-SiC film was also tested by attaching DNA [70]. The probe DNA was labeled with a redox center of ferrocene moiety. The complementary DNA was labeled with a red fluorescent marker of Cy5 dye. As shown in Figure 1.9a, the fluorescence image of a bare 3C-SiC film shows no emission of red light, indicating no adsorption of DNA on the surface of the film. After electrochemical grafting of a nitrophenyl layer and further hybridization of probe DNA with complementary DNA onto the nanocrystalline 3C-SiC surface, the functionalized area showed a high intensity of red fluorescence, indicating complementary DNA has been immobilized. The voltammogram of probe

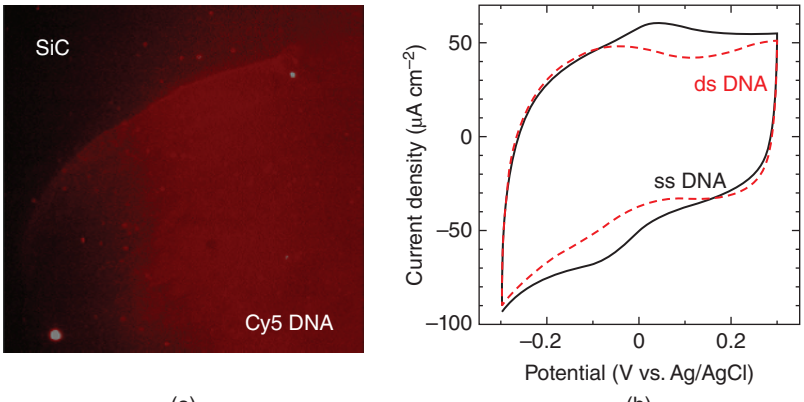

Figure 1.9 (a) Fluorescence microscopy image of a double-stranded DNA functionalized SiC electrode, and (b) cyclic voltammograms of single-stranded DNA (solid line) and double-stranded DNA (dashed line) modified 3C-SiC film in pH 7.4 phosphate buffer at a scan rate of 50 mV s^{-1} [70]. Source: Reprinted with permission from ACS Publisher, Copyright 2011.

DNA (single-stranded DNA) immobilized 3C-SiC film (Figure 1.9b) showed a couple of redox waves of ferrocene moiety centered at $E_{1/2} = 0 \pm 5$ mV (vs. Ag/AgCl) and with ΔE of 50 ± 10 mV. These waves became smaller or even disappeared after hybridizing the probe DNA with complementary DNA (double-stranded DNA). A decrease in the redox current specifically indicates the presence of complementary DNA. Since the hybridized DNA has increased rigidity, the access of the terminal ferrocene moiety to the 3C-SiC surface is thus inhibited, leading to a reduced or absent redox current from the ferrocene moiety of probe DNA. This method was simple, since either labeling target DNAs or adding external electroactive species were needed.

The label-free electrical detection of DNA molecules has been reported using SiC nanowire based field effect transistors (NWFETs) [105]. Non-intentionally n-doped SiC NWs with a length of approximately 2 μm and a diameter ranging from 25 to 60 nm were grown using a bottom-up vapor–liquid–solid mechanism. The SiC NWFETs were fabricated and further functionalized with DNA molecules via covalent coupling of an amino-terminated organosilane. The drain current vs. drain voltage characteristics obtained after the DNA grafting and hybridization were measured and compared. As a representative result, the current was lowered by 22% after probe DNA grafting, and by 7% after target DNA hybridization. The current decrease confirmed the field effect induced by the negative charges of DNA molecules. Moreover, the selectivity, reproducibility, reversibility, and stability of the NWFET devices were studied by dehybridization, non-complementary hybridization, and rehybridization experiments. This first proof of concept opens the way for future developments using SiC-NW based sensors [105].

1.4.3 Energy Storage

SiC has been employed for the construction of supercapacitors and batteries as well as for the loading of catalysts. For example, an electrochemical capacitor was constructed using a nanocrystalline 3C-SiC film. This is because the nanocrystalline 3C-SiC film

shows not only a relatively high double layer capacitance (40–100 μF cm^{-2}, depending on the growth conditions), but also long-term stability of its capacitance. Moreover, SiC features high thermal and long-term chemical stability in harsh physicochemical environments [65, 106, 107]. Figure 1.10a depicts the cyclic voltammetric curves of nanocrystalline 3C-SiC film in 0.1 M H_2SO_4 at different scan rates [16]. For all the scan rates considered, the quasi-rectangular shape of the curves is clearly observable in the potential range scanned. The curves are symmetric, as expected for a typical electrical double layer capacitor (EDLC). Its charging–discharging behavior at different current densities (4–80 μA cm^{-2}) is shown in Figure 1.10b. For all current densities tested, the anodic charging segment is symmetric to the cathodic discharging counterpart, indicating the high reversibility of this EDLC. Its specific capacitance was calculated to be 70 μF cm^{-2} at a scan rate of 10 mV s^{-1}. Nevertheless, only 34% reduction in its capacitance is observed, even with a 20-fold increase in the scan rate. As summarized in Figure 1.10c, the specific capacitance decreases by only 25% (from 65 to 43 μF cm^{-2}) in the case of altering charging current density from 4 to 80 μA cm^{-2}. Therefore, an

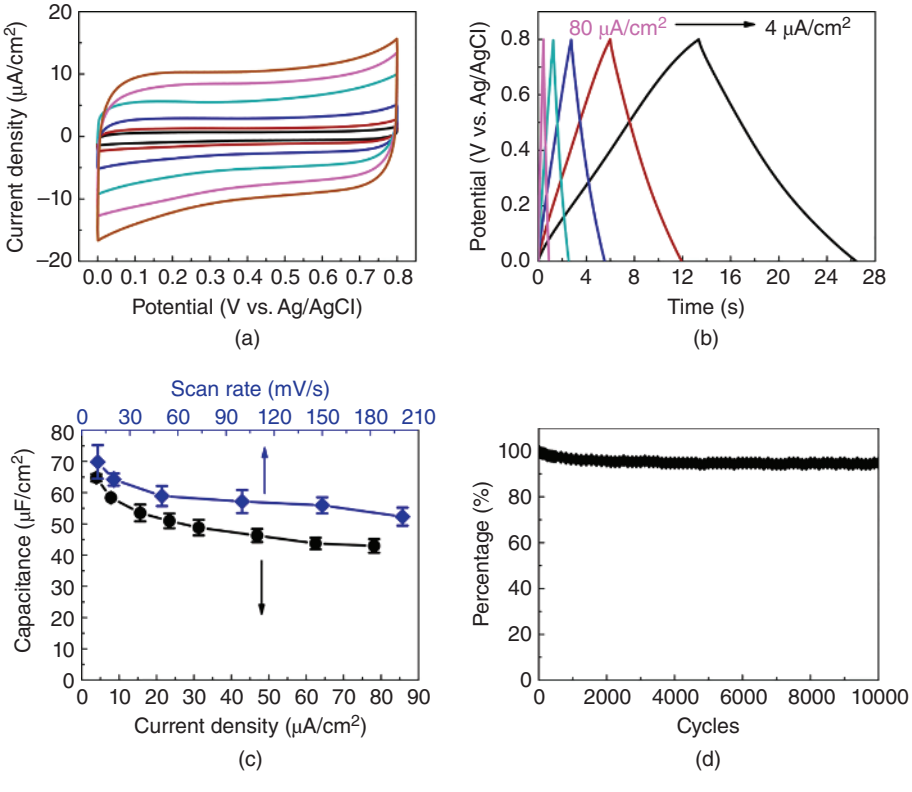

Figure 1.10 The performance of a nanocrystalline 3C-SiC film based EDLC in 0.1 M H_2SO_4: (a) cyclic voltammetric curves at different scan rates, from inside to outside: 10–200 mV s^{-1}; (b) charging–discharging curves with different current densities; (c) specific capacitance as a function of scan rates and charging current densities; (d) the variation of capacitance with charging–discharging cycles. The current densities were normalized with the real surface area of the nanocrystalline 3C-SiC film [16]. Source: Reprinted with permission from ACS Publisher, Copyright 2012.

excellent rate performance has been achieved on the nanocrystalline 3C-SiC film based EDLC. In addition to its high specific capacitance, the cyclic stability of the 3C-SiC film based EDLC was examined. As shown in Figure 1.10d, the nanocrystalline 3C-SiC retains 94.8% of its initial capacitance after 10 000 cycles. These results are comparable with those constructed using carbon materials (>80%) [108, 109], indicating a very high cyclic stability of the nanocrystalline 3C-SiC film based EDLC.

To further improve the capacitances of SiC-based supercapacitors, the usage of thin SiC films with high geometric areas or SiC nanostructures (e.g. wires, particles, etc.) has been proposed. For example, an activated carbon-derived SiC nanoparticle showed a specific capacitance of 114.7 F g^{-1} at a current density of 0.12 A g^{-1} [110]. A CVD-fabricated SiC NW showed an areal capacitance of 240 μF cm^{-2} at a scan rate of 100 mV s^{-1} [111]. In 0.1 M H_2SO_4 solution, a 3C-SiC NW synthesized on graphite paper (GP) by a carbothermal reduction method exhibited specific capacitances of 25.6, 37, 28, and 28 mF cm^{-2} at current densities of 0.2, 0.3, 0.5, and 2.0 A cm^{-2}, respectively. These values remained unchanged even after 2000 cycles, showing excellent capacitance retention [112]. A SiC nanocauliflower featured a specific capacitance of up to ~300 F g^{-1} at a scan rate of 5 mV s^{-1}. With a working voltage of 1.8 V, a fabricated symmetric supercapacitor device delivered a specific capacitance of 188 F g^{-1} at a scan rate of 5 mV s^{-1}, capacitance retention of 97.05% after 30 000 cycles, an energy density of 31.43 W h kg^{-1}, and a power density of ~18.8 kW kg^{-1} at 17.76 W h kg^{-1} [113, 114]. However, it is still a great challenge to fully utilize active SiC electrode materials [114–116]. Further integrating SiC nanostructures with other metal oxides or conducting polymers is proving to be an alternative approach for further enhancement of the performance of SiC-based supercapacitors. For example, coating SiC NWs with $Ni(OH)_2$ and MnO_2 improved the specific capacitances up to 1724 and 273.2 F g^{-1}, respectively [117, 118].

Besides electrochemical capacitors, SiC films have been identified as possible anode materials for rechargeable lithium batteries [119–121]. Note that SiC bulk is generally regarded as electrochemically inactive in lithium-ion batteries (LIBs). However, very recently, a few reports revealed that SiC could serve as an anode material for LIBs. For example, a nanocrystalline SiC film grown on metallic current collector substrates by means of modified PECVD exhibited a reversible reaction with Li ions [119]. The CVD-grown SiC film consisted of nanocrystalline 4H-SiC surrounded by amorphous SiC networks. As the anode, such a film exhibited a specific discharging capacity of 309 mA h g^{-1}, which was stable over 60 cycles at different charging and discharging rates. The formation of Li_4C layers in lithiation was proposed. Cubic nano-SiC, prepared by a CVD method, has also been used as an anode for lithium insertion. A reversible lithium insertion was reported with a capacity of about 1200 mA h g^{-1} over 200 cycles [120]. Bead-curtain shaped, SiC-coated SiO_2 (by convention, SiC@SiO_2) core-shell nanowires (SiC@SiO_2-CSNWs) have been synthesized on GP [121]. Bare SiC NWs (SiCNWs) were also fabricated on GP. These as-prepared SiCNWs and SiC@SiO_2-CSNWs (without addition of binder or electron conductive materials) were directly used as working electrodes for lithium batteries. For example, SiCNWs exhibited high specific capacities and good cycling stabilities, ascribed to the unique NW structure, effectively buffering volume changes upon repeated alloying and de-alloying. Comparatively, SiC@SiO_2-CSNWs presented much better electrochemical properties. The conducted intensive TEM and FTIR measurements revealed that the SiO_2 shell effectively separated the direct contact between active SiC and the electrolyte, thus

suppressing the rapid growth of solid electrolyte interface film in repeated cycling, and stabilized the structure of active material [121]. SiC@Si core-shell NWs have been synthesized on carbon paper via a two-step CVD method. Without any additional binder, they have been further employed as a hybrid anode for lithium-ion batteries [122]. Silicon was selected because it is considered one of the most promising anode materials for next-generation LIBs due to its high theoretical capacity. However, its large volume changes during electrochemical cycling limit its commercial application. The synthesized SiC@Si NWs exhibit high specific capacity, high coulombic efficiency, and good cycling stability. After 50 cycles, the discharge capacities remained 2837 and 1809 mAh g^{-1} at rates of 0.1 and 0.5 C, respectively. The influence of the growth time of SiC NWs and the thickness of Si film on the performance of LIBs was also considered [122].

Combining these results with the high cyclic stability of SiC films and nanostructures, one can believe that they are very promising candidates for the construction of stable, reversible, and long lifetime capacitors and batteries. There is tremendous potential for SiC films and their nanostructures as electrodes in energy storage and conversion applications.

1.4.4 Other Applications

SiC films and their nanostructures have been used for electrocatalytic and related applications. For example, core-shell structured SiC@C (namely a nanoscale SiC core and a graphitic carbon shell) has been used as a support to load electrocatalysts for direct methanol fuel cells [123]. The SiC@C was prepared by graphitization of nano-SiC under a vacuum of 10^{-3} Pa at 1500°C. The epitaxially grown carbon layer had a high conductivity and an affinity for Pt metal catalysts, while the SiC core retained its high stability. Pt electrocatalysts supported on SiC@C (Pt/SiC@C) were prepared using a microwave heating method. The Pt/SiC@C electrocatalyst had much higher catalytic activities than the Pt/SiC electrocatalyst toward methanol electro-oxidation and oxygen reduction reactions. More significantly, the Pt/SiC@C electrocatalyst showed greater stability in comparison with the traditional Pt/C. The superior electrocatalytic performance of Pt/SiC@C has been ascribed to a high dispersion of Pt nanoparticles on the SiC@C support, and high stability of the SiC@C support in acid solutions.

Bio-inspired N-doped SiC/Mo composite has proved to be a green and cost-effective alternative for practical desulfurization of fuel [124]. This is because MoO_2, Mo_2C, and $MoSi_2$ particles dispersed well on the surface of N-doped SiC composite. It has shown superior catalytic properties in oxidative desulfurization of model fuel (99.6%).

1.5 Conclusions

By use of different techniques and under different growth conditions (e.g. growth temperature, power density, precursor, etc.), various 3C-SiC films and nanostructures have been grown. These materials feature changed properties, ranging from their morphology (e.g. crystallinity, defects, phase composition, roughness, etc.), conductivities, and interfacial properties (e.g. surface reactivity, capacitive and faradaic behavior, etc.). The structural heterogeneity of SiC films actually determines their properties. For example,

surface conditions of the SiC films (e.g. crystal orientation, composition, surface functional groups, etc.) drastically affect the formation of electrical double layers and charge transfer kinetics during electrochemical processes. Therefore, the performance of the applications (e.g. detection limits for electrochemical sensing, capacitances for electrochemical capacitors, etc.) of different SiC films and nanostructures is varied. For example, a high-performance supercapacitor and a sensitive dopamine electrochemical sensor were demonstrated using a nanocrystalline 3C-SiC film and an epitaxial 3C-SiC film, respectively.

However, more detailed and in-depth studies are still required in order to explore various SiC films and nanostructures for different applications. Regarding the growth of SiC films and their nanostructures, currently established methods always involve toxic reagents and solvents. Moreover, some byproducts always remain that might limit the overall performance of SiC materials, especially SiC nanomaterials. With respect to the characterization and property investigation of SiC films and their nanostructures, most of them are only qualitatively discussed. Quantitative studies are of course needed in some cases to distinguish clearly their property differences (e.g. crystallinity, crystal orientation, phase composition, defects, roughness, surface reactivity, surface functional groups, capacitive and faradaic behavior, etc.). For example, the sources of the conductivities of various SiC films, as well as how to further improve or tune their conductivities, have to be clarified. Doping of SiC films and their nanostructures with different dopants needs to be conducted, and their conductivities as well as electrochemistry (e.g. electrochemical potential window, double-layer capacitance, and redox activity, etc.) should be investigated. To compare with previously reported robust electrodes such as boron-doped diamond electrodes, the effects of surface termination, the conductivities (resulting from dopants and doping levels), and crystal structures/polytypes of SiC films on the electrochemical properties of SiC films and nanostructures need to be investigated. The stability of SiC films and their nanostructures at high positive potentials or with strong oxidative reactants (namely the oxidation of silicon atoms on the surface of SiC films and their nanostructures), various approaches to modify SiC films and their nanostructures by use of silicone and/or carbon chemistry (more exactly the reaction sites – carbon or silicon atoms during functionalization processes), and the employment of functionalized SiC surfaces for electrochemical and biochemical applications should be considered. As for the applications of SiC films and their nanostructures, more strategies are still needed. Taking the construction of SiC-based supercapacitors as an example, only the surfaces of active SiC materials contribute efficiently to the total capacitance, while most of SiC materials below the surface do not take part in the electrochemical processes, leading to lower specific capacitances than expected. For SiC-based lithium batteries, the interaction of lithium ions with active SiC materials has not been clarified. For the biosensors and biointerfaces based on SiC films and their nanostructures, more experiments are still required to evaluate their performance with respect to sensitivity, stability, and detection limits. In particular we require more knowledge of the reaction efficiency of SiC films and their nanostructures with biomolecules (e.g. DNA), investigation of the linker density, and the reaction conditions (e.g. reaction time, reaction temperature, the concentration and amount of biomolecules, etc.).

In summary, SiC films and their nanostructures are fantastic materials featuring many unique physical and chemical properties. More applications of SiC films and

their nanostructures in different fields are highly expected, such as in the fields of electrochemical and biochemical sensing as well as electrochemical energy storage and conversion.

Acknowledgements

The authors acknowledge financial support from the German Research Foundation (DFG) under project YA344/1-1.

References

1 Berzelius, J.J. (1824). Unterfuchungiiber die Flufsfpathaure und deven merkwiirdigften Verbindungen. *Ann. Phys.* (Leipzig, Ger.) 1: 169–192.
2 Moissan, H. (1905). Étude du siliciure de carbone de la météorite de Cañon Diablo. *C. R. Acad. Sci.* 140: 405–406.
3 Choyke, W.J., Matsunami, H., and Pensl, G. (eds.) (2004). *Silicon Carbide: Recent Major Advances*. Berlin: Springer.
4 Pedersen, H., Leone, S., Kordina, O. et al. (2012). Chloride-based CVD growth of silicon carbide for electronic applications. *Chem. Rev.* 112: 2434–2453.
5 Jiang, L. and Cheung, R. (2009). A review of silicon carbide development in MEMS applications. *Int. J. Comput. Mater. Sci. Surf. Eng.* 2: 225–240.
6 Muranaka, T., Kikuchi, Y., Yoshizawa, T. et al. (2009). Superconductivity in carrier-doped silicon carbide. *Sci. Technol. Adv. Mater.* 9: 044204.
7 Round, H.J. (1907). A note on carborundum. *Electr. World* 19: 309.
8 CRC (2010–2011). *Handbook of Chemistry and Physics*, 91e, 12–212. Boca Raton, FL: CRC Press.
9 Berger, C., Song, Z., Li, X. et al. (2006). Electronic confinement and coherence in patterned epitaxial graphene. *Science* 312: 1191–1196.
10 Melinon, P., Masenelli, B., Tournus, F., and Perez, A. (2007). Growth and chemical applications of SiC: playing with silicon and carbon atoms at the nanoscale. *Nat. Mater.* 6: 479–490.
11 Su, S.-P., Wu, C.-L., Cheng, C.-H. et al. (2016). Nonstoichiometric SiC bus/ring waveguide based all-optical data format follower and inverter. *ACS Photonics* 3: 806–818.
12 Oliveros, A., Guiseppi-Elie, A., and Saddow, S.E. (2013). Silicon carbide: a versatile material for biosensor applications. *Biomed. Microdevices* 15: 353–368.
13 Frewin, C.L., Coletti, C., Register, J.J. et al. (2014). Silicon carbide materials for biomedical applications. In: *Carbon for Sensing Devices* (ed. D. Demarchi and A. Tagliaferro), 153–207. Cham: Springer.
14 Wu, R., Zhou, K., Yue, C.Y. et al. (2015). Recent progress in synthesis, properties and potential applications of SiC nanomaterials. *Prog. Mater. Sci.* 72: 1–60.
15 Fend, Z.C. (2004). *SiC Power Materials: Devices and Applications in Material Science*. Berlin: Springer-Verlag.

16 Zhuang, H., Yang, N., Zhang, L. et al. (2015). Electrochemical properties and applications of nanocrystalline, microcrystalline, and epitaxial cubic silicon carbide films. *ACS Appl. Mater. Interfaces* 7: 10886–10895.
17 Schwetk, K.A., Werheit, H., and Nold, E. (2003). Sintered and monocrystalline black and green silicon carbide: chemical compositions and optical properties. *Ceram. Forum Int.* 80: D32+E37-.
18 Augustin, G., Balakrishna, V., and Brandt, C.D. (2000). Growth and characterization of high-purity SiC single crystals. *J. Cryst. Growth* 211: 339–342.
19 Semmelroth, K., Schulze, N., and Pensl, G. (2004). Growth of SiC polytypes by the physical vapour transport technique. *J. Phys. Condens. Matter* 16: S1597–S1610.
20 Lely, J.A. and Keram, B.D. (1995). Darstellung von Einkristallen von Silizium Karbide und Beherrschung von Art und Menge der eingebauten Verunreinigungen. *Berichte der Deutschen Keramischen Gesellschaft* 32: 229–231.
21 Tairov, M.Y. and Tsvetkov, V.F. (1978). Investigation of growth processes of ingots of silicon carbide single crystals. *J. Cryst. Growth* 43: 209–212.
22 Straubinger, T.L., Bickermann, M., Weingaertner, R. et al. (2002). Aluminum p-type doping of silicon carbide crystals using a modified physical vapor transport growth method. *J. Cryst. Growth* 240: 117–123.
23 Wellmann, P., Desperrier, P., Müller, R. et al. (2005). SiC single crystal growth by a modified physical vapor transport technique. *J. Cryst. Growth* 275: e555–e560.
24 Kavcký, Š., Aneková, B., Madejová, J., and Šajgalík, P. (2000). Silicon carbide powder synthesis by chemical vapor deposition from siliane/acetylene reaction system. *J. Eur. Ceram. Soc.* 20: 1939–1946.
25 Zorman, C.A., Fu, X.A., and Mehregany, M. (2006). *Deposition Techniques for SiC MEMS, Silicon Carbide MEMS for Harsh Environments*. London: Imperial College Press.
26 Nishino, S., Powell, J.A., and Will, H.A. (1983). Production of large-area single-crystal wafers of cubic SIC for semiconductor devices. *Appl. Phys. Lett.* 42: 460–462.
27 Powell, J.A., Matus, L.G., and Kuczmarski, M.A. (1987). Growth and characterisation of cubic SiC single-crystal films on Si. *J. Electrochem. Soc.* 134: 1558–1565.
28 Zorman, C.A., Fleischman, A.J., Dewa, A.S. et al. (1995). Epitaxial growth of 3C-SiC films on 4 in diam (100) silicon wafers by atmospheric pressure chemical vapor deposition. *J. Appl. Phys.* 78: 5136–5138.
29 G. Krotz, W. Legner, H. Moller, et al. 1995, Silicon carbide as a mechanical material, Proceedings of the 8th International Conference Solid State Sensors Actuators – Eurosensors IX, p. 186.
30 Boo, J.H., Lee, S.B., Yu, K.S. et al. (2000). High vacuum chemical vapour deposition of cubic SiC thin films on Si (001) substrates using single source precursor. *Surf. Coat. Technol.* 131: 147–152.
31 Chen, J., Scofield, J., and Steckl, A.J. (2000). Formation of SiC SOI structures by direct growth on insulating layers. *J. Electrochem. Soc.* 147: 3845–3849.
32 Clavaguera-Mora, M.T., Rodriguez-Viejo, J., El Felk, Z. et al. (1997). Growth of SiC films obtained by LPCVD. *Diamond Relat. Mater.* 6: 1306–1310.

33 Hurtos, E. and Rodriguez-Viejo, J. (2000). Residual stress and texture in poly-SiC films grown by low-pressure organometallic chemical-vapor deposition. *J. Appl. Phys.* 87: 1748–1757.

34 Lee, K.S., Park, J.Y., Kim, W.J., and Hong, G.W. (2001). Effect of microstructure of SiC layer on the indentation properties of silicon carbide-graphite system fabricated by LPCVD method. *J. Mater. Sci. Lett.* 20: 1229–1231.

35 Wijesundara, M.B.J., Stoldt, C.R., Carraro, C. et al. (2002). Nitrogen doping of polycrystalline 3C-SiC films grown by single-source chemical vapor deposition. *Thin Solid Films* 419: 69–75.

36 Roper, C.S., Howe, R.T., and Maboudian, R. (2006). Stress control of polycrystalline 3C-SiC films in a large-scale LPCVD reactor using 1,3-disilabutane and dichlorosilane as precursors. *J. Micromech. Microeng.* 16: 2736–2739.

37 Beisenov, R., Ebrahim, R., Mansurov, Z.A. et al. (2013). Growth of 3C-SiC films on Si (111) and sapphire (0001) substrates by MOCVD. *Eurasian Chem. Technol. J.* 15: 25–29.

38 Flannery, A.F., Mourlas, N.J., Storment, C.W. et al. (1998). PECVD silicon carbide as a chemically resistant material for micromachined transducers. *Sens. Actuators, A* 70: 48–55.

39 Sarro, P., de Boer, C.R., Korkmaz, E., and Laros, J.M.W. (1998). Low-stress PECVD SiC thin films for IC-compatible microstructures. *Sens. Actuator, A* 67: 175–180.

40 Klumpp, A., Schaber, U., Offereins, H.L. et al. (1994). Amorphous SiC and its application in silicon micromachining. *Sens. Actuators, A* 41-42: 310–316.

41 Henry, A., Hassan, J., Bergman, J.P. et al. (2006). Thick silicon carbide homoepitaxial layers grown by CVD techniques. *Chem. Vap. Deposition* 12: 475–482.

42 Ellison, A., Zhang, J., Henry, A., and Janzen, E. (2002). Epitaxial growth of SiC in a chimney CVD reactor. *J. Cryst. Growth* 236: 225–238.

43 Kordina, O., Hallin, C., Ellison, A. et al. (1996). High temperature chemical vapor deposition of SiC. *Appl. Phys. Lett.* 69: 1456–1458.

44 Ito, M., Storasta, L., and Tsuchida, H. (2008). Development of 4H-SiC epitaxial growth technique achieving high growth rate and large-area uniformity. *Appl. Phys. Express* 1: 015001.

45 Tsuchida, H., Ito, M., Kamata, I., and Nagano, M. (2009). Formation of extended defects in 4H-SiC epitaxial growth and development of a fast growth technique. *Phys. Status Solidi B* 246: 1553–1568.

46 Ishida, Y., Takahashi, T., Okumura, H. et al. (2009). Development of a practical high-rate CVD system. *Mater. Sci. Forum* 600–603: 119–122.

47 Yang, B., Zhuang, H., Li, J. et al. (2016). Defect-induced strain relaxation in 3C-SiC films grown on a (100) Si substrate at low temperature in one step. *CrystEngComm* 18: 6817–6823.

48 Nagasawa, H., Yagi, K., and Kawahara, T. (2002). 3C-SiC hetero-epitaxial growth on undulant Si(001) substrate. *J. Cryst. Growth* 237–239: 1244–1249.

49 Wrobel, A.M., Walkiewicz-Pietrzykowska, A., and Uznanski, P. (2014). Remote hydrogen microwave plasma chemical vapor deposition from methylsilane precursors. 1. Growth mechanism and chemical structure of deposited a-SiC:H films. *Thin Solid Films* 564: 222–231.

50 Zhu, P., Xu, Q., Chen, R. et al. (2017). Structural study of β-SiC(001) films on Si(001) by laser chemical vapor deposition. *J. Am. Ceram. Soc.* 100: 1634–1641.

51 Liu, X.F., Yan, G.G., Shen, Z.W. et al. (2017). A facile method for heteroepitaxial growth of homogeneous 3C-SiC thin films on both surfaces of suspended Si wafer by conventional chemical vapor deposition. *ECS J. Solid State Sci. Technol.* 6: P27–P31.

52 Zhuang, H., Zhang, L., Staedler, T., and Jiang, X. (2013). Low temperature hetero-epitaxial growth of 3C-SiC films on Si utilizing microwave plasma CVD. *Chem. Vap. Deposition* 19: 29–37.

53 Wang, C., Huang, N., Zhuang, H. et al. (2016). Growth of large-scale heteroepitaxial 3C-SiC films and nanosheets on silicon substrates by microwave plasma enhanced CVD at higher powers. *Surf. Coat. Technol.* 299: 96–103.

54 Tu, R., Zheng, D., Cheng, H. et al. (2017). Effect of $CH_4/SiCl_4$ ratio on the composition and microstructure of ⟨110⟩ oriented β-SiC bulks by halide CVD. *J. Eur. Ceram. Soc.* 37: 1217–1223.

55 Zhao, Z., Li, Y., Yin, Z., and Li, Z. (2016). Effect of C/Si ratio on the characteristics of 3C-SiC films deposited on Si(100) base on the four-step non-cooling process. *Superlattices Microstruct.* 99: 131–135.

56 Zhang, L., Zhuang, H., Jia, C.L., and Jiang, X. (2015). Role of catalyst in controlling the growth and morphology of one-dimensional SiC nanostructures. *CrystEngComm* 17: 7070–7078.

57 Zhuang, H., Zhang, L., Fuchs, R. et al. (2013). When epitaxy meets plasma: a path to ordered nanosheets arrays. *Sci. Rep.* 3: 2427.

58 Zhuang, H., Zhang, L., Staedler, T., and Jiang, X. (2011). Highly selective diamond and β-SiC crystal formation at increased atomic hydrogen concentration: a route for synthesis of high-quality and patterned hybrid diamond/β-SiC composite film. *Scr. Mater.* 65: 548–551.

59 Sasaki, Y., Nishina, Y., Sato, M., and Okamura, K. (1987). Raman-study of SiC fibers made from polycarbosilane. *J. Mater. Sci.* 22: 443–448.

60 Inoue, Y., Nakashima, S., Mitsuishi, A. et al. (1983). Raman spectra of amorphous SiC. *Solid State Commun.* 48: 1071–1075.

61 Catherine, Y., Zamouche, A., Bullot, J., and Gauthier, M. (1983). Ion bombardment effects in plasma deposition of hydrogenated amorphous silicon carbide films: a comparative study of D.C. and R.F. discharges. *Thin Solid Films* 109: 145–158.

62 Dutta, R., Banerjee, P.K., and Mitra, S.S. (1982). Effect of hydrogenation on the electrical conductivity of amorphous silicon carbide. *Solid State Commun.* 42: 219–222.

63 Bullot, J. and Schmidt, M.P. (1987). Physics of amorphous silicon-carbon alloys. *Phys. Status Solidi B* 143: 345–418.

64 Nagasawa, H., Yagi, K., Kawahara, T., and Hatta, N. (2006). Reducing planar defects in 3C-SiC. *Chem. Vap. Deposition* 12: 502–508.

65 Abderrazak, H. and Hmida, E.S.B.H. (2011). Silicon carbide: synthesis and properties. In: *Properties and Applications of Silicon Carbide* (ed. R. Gerhardt), 361–388. London: IntechOpen.

66 Hume, D.N. and Kolthoff, I.M. (1941). The silicon carbide electrode. *J. Am. Chem. Soc.* 63: 2805–2806.

67 Godignon, P. (2005). SiC materials and technologies for sensors development. *Mater. Sci. Forum* 483–485: 1009–1014.

68 Carter, C.H. Jr.,, Glass, R., Brady, M. et al. (2001). Germanium on SiC(0001): surface structure and nanocrystals. *Mater. Sci. Forum* 353–356: 353–356.

69 Eickhoff, M., Möller, H., Stoemenos, J. et al. (2004). Influence of crystal quality on the electronic properties of n-type 3C-SiC grown by low temperature, low pressure chemical vapor deposition. *J. Appl. Phys.* 95: 7908–7917.

70 Yang, N., Zhuang, H., Hoffmann, R. et al. (2011). Nanocrystalline 3C-SiC electrode for biosensing applications. *Anal. Chem.* 83: 5827–5830.

71 Song, X., Michaud, J.F., Cayrel, F. et al. (2010). Evidence of electrical activity of extended defects in 3C-SiC grown on Si. *Appl. Phys. Lett.* 96: 142104.

72 Tsuboi, H., Kabasawa, M., Ouchi, S. et al. (2009). Computational evaluation of electrical conductivity on SiC and the influence of crystal defects. *Mater. Sci. Forum* 600–603: 497–500.

73 Dasgupta, D., Demichelis, F., and Tagliaferro, A. (1991). Electrical conductivity of amorphous carbon and amorphous hydrogenated carbon. *Philos. Mag. B* 63: 1255–1266.

74 Demichelis, F., Pirri, C.F., Tresso, E. et al. (1991). Physical properties of undoped and doped hydrogenated amorphous silicon carbide. *Semicond. Sci. Technol.* 6: 1141–1146.

75 Raffy, G., Furthmüller, J., Wagner, J.M., and Bechstedt, F. (2004). Ab initio study of structural and electronic properties of planar defects in Si and SiC. *Phys. Rev. B* 70: 195344.

76 Na, H., Kim, H., Adachi, K. et al. (2004). High-quality schottky and ohmic contacts in planar 4H-SiC metal semiconductor field-effect transistors and device performance. *J. Electron. Mater.* 33: 89–93.

77 Dhar, S., Seitz, O., Halls, M.D. et al. (2009). Chemical properties of oxidized silicon carbide surfaces upon etching in hydrofluoric acid. *J. Am. Chem. Soc.* 131: 16808–16813.

78 Yang, N., Zhuang, H., Hoffmann, R., Smirnov, W.,Hees, J., Jiang, X., Nebel, C.E. Electrochemistry of Nanocrystalline 3C-SiCFilms, *Chemistry – A European Journal* 2012, 18(21): 6514–6519.

79 Sachsenhauser, M., Sharp, I.D., Stutzmann, M., and Garrido, J.A. (2016). Surface state mediated electron transfer across the n-type SiC/electrolyte interface. *J. Phys. Chem. C* 120: 6524–6533.

80 Sachsenhauser, M., Walczak, K., Hampel, P.A. et al. (2016). Suppression of photoanodic surface oxidation of n-type 6H-SiC electrodes in aqueous electrolytes. *Langmuir* 32: 1637–1644.

81 Ballarin, N., Carraro, C., Maboudian, R., and Magagnin, L. (2014). Electropolishing of n-type 3C-polycrystalline silicon carbide. *Electrochem. Commun.* 40: 17–19.

82 Yakimova, R., Petoral, R.M. Jr.,, Yazdi, G.R. et al. (2007). Surface functionalization and biomedical applications based on SiC. *J. Phys. D: Appl. Phys.* 40: 6435–6442.

83 Schoell, S.J., Hoeb, M., Sharp, I.D. et al. (2008). Functionalization of 6H-SiC surfaces with organosilanes. *Appl. Phys. Lett.* 92: 153301.

84 Rosso, M., Arafat, A., Schroën, K. et al. (2008). Covalent attachment of organic monolayers to silicon carbide surfaces. *Langmuir* 24: 4007–4012.

85 Steenackers, M., Sharp, I.D., Larsson, K. et al. (2010). Structured polymer brushes on silicon carbide. *Chem. Mater.* 22: 272–278.

86 Rosso, M., Giesbers, M., Arafat, A. et al. (2009). Covalently attached organic monolayers on SiC and Si_xN_4 surfaces: formation using UV light at room temperature. *Langmuir* 25: 2172–2180.

87 Iijima, M. and Kamiya, H. (2008). Surface modification of silicon carbide nanoparticles by azoradical initiators. *J. Phys. Chem. C* 112 (2008): 11786–11790.

88 Hody, H., Pireaux, J.-J., Choquet, P., and Moreno-Couranjou, M. (2010). Plasma functionalization of silicon carbide crystalline nanoparticles in a novel low pressure powder reactor. *Surf. Coat. Technol.* 205: 22–29.

89 Tengeler, S., Kaiser, B., Ferro, G. et al. (2018). The (001) 3C-SiC surface termination and band structure after common wet chemical etching procedures, stated by XPS, LEED, and HREELS. *Appl. Surf. Sci.* 427: 480–485.

90 Seyller, T. (2004). Passivation of hexagonal SiC surfaces by hydrogen termination. *J. Phys. Condens. Matter* 16: S1755–S1782.

91 Sieber, N., Manel, B.F., Seyller, T. et al. (2001). Electronic and chemical passivation of hexagonal 6H-SiC surfaces by hydrogen termination. *Appl. Phys. Lett.* 78: 1216.

92 Schoell, S., Howgate, J., Hoeb, M. et al. (2011). Electrical passivation and chemical functionalization of SiC surfaces by chlorine termination. *Appl. Phys. Lett.* 98: 182106.

93 Pujari, S.P., Scheres, L., Weidner, T. et al. (2013). Covalently attached organic monolayers onto silicon carbide from 1-alkynes: molecular structure and tribological properties. *Langmuir* 29: 4019–4031.

94 Schoell, S.J., Sachsenhauser, M., Oliveros, A. et al. (2013). Organic functionalization of 3C-SiC surfaces. *ACS Appl. Mater. Interfaces* 5: 1393–1399.

95 Auernhammer, M., Schoell, S., Sachsenhauser, M. et al. (2012). Surface functionalization of 6H-SiC using organophosphonate monolayers. *Appl. Phys. Lett.* 100: 101601.

96 H. Zhuang, X. Jiang, Allylamine functionalization of 3C-SiC thin film, Proceedings of the 8th Pacific Rim International Congress on Advanced Materials and Processing (2013)1853–1861.

97 Brooksby, P.A. and Downard, A.J. (2004). Electrochemical and atomic force microscopy study of carbon surface modification via diazonium reduction in aqueous and acetonitrile solutions. *Langmuir* 20: 5038–5045.

98 Allongue, P., Delamar, M., Desbat, B. et al. (1997). Covalent modification of carbon surfaces by aryl radicals generated from the electrochemical reduction of diazonium salts. *J. Am. Chem. Soc.* 119: 201–207.

99 Ortiz, B., Saby, C., Champagne, G.Y., and Belanger, D. (1998). Electrochemical modification of a carbon electrode using aromatic diazonium salts. 2. Electrochemistry of 4-nitrophenyl modified glassy carbon electrodes in aqueous media. *J. Electroanal. Chem.* 455: 75–81.

100 Uetsuka, H., Shin, D., Tokuda, N. et al. (2007). Electrochemical grafting of boron-doped single-crystalline chemical vapor deposition diamond with nitrophenyl molecules. *Langmuir* 23: 3466–3472.

101 Zhuang, H., Wang, C., Huang, N., and Jiang, X. (2014). Cubic SiC for trace heavy metal ion analysis. *Electrochem. Commun.* 41: 5–7.

102 Smirnov, W., Yang, N., Hoffmann, R. et al. (2011). Integrated all-diamond ultramicroelectrode arrays: optimization of faradaic and capacitive currents. *Anal. Chem.* 83: 7438–7443.

103 Walsh, F.X., Stevens, T.J., Langlais, P.J., and Bird, E.D. (1982). Dopamine and homovanillic acid concentrations in striatal and limbic regions of human brain. *Ann. Neurol.* 12: 52–55.

104 Wilk, S. and Stanley, M. (1978). Dopamine metabolites in human brain. *Psychopharmacology* 57: 77–81.

105 Fradetal, L., Bano, E., Attolini, G. et al. (2016). A silicon carbide nanowire field effect transistor for DNA detection. *Nanotechnology* 27: 235501.

106 Lin, H., Gerbec, J.A., Sushchikh, M., and McFarland, E.W. (2008). Synthesis of amorphous silicon carbide nanoparticles in a low temperature low pressure plasma reactor. *Nanotechnology* 19: 325601.

107 Zhuang, H., Zhang, L., Staedler, T., and Jiang, X. (2012). Nanoscale integration of SiC/SiO_2 core-shell nanocables in diamond through a simultaneous hybrid structure fabrication. *Appl. Phys. Lett.* 100: 193102.

108 Ania, C.O., Khomenko, V., Raymundo-Piñero, E. et al. (2007). The large electrochemical capacitance of microporous doped carbon obtained by using a zeolite template. *Adv. Funct. Mater.* 17: 1828–1836.

109 Zhang, L.L. and Zhao, X.S. (2009). Carbon-based materials as supercapacitor electrodes. *Chem. Soc. Rev.* 38: 2520–2531.

110 Sarno, M., Galvagno, S., Piscitelli, R. et al. (2016). Supercapacitor electrodes made of exhausted activated carbon derived SiC nanoparticles coated by graphene. *Ind. Eng. Chem. Res.* 55: 6025–6035.

111 Carraro, C. and Maboudian, R. (2013). Silicon carbide nanowires as highly robust electrodes for micro-supercapacitors. *J. Power Sources* 230: 298–302.

112 Chen, J., Zhang, J., Wang, M. et al. (2014). SiC nanowire film grown on the surface of graphite paper and its electrochemical performance. *J. Alloys Compd.* 605: 168–172.

113 Sanger, A., Kumar, A., Kumar, A. et al. (2016). Silicon carbide nanocauliflowers for symmetric supercapacitor devices. *Ind. Eng. Chem. Res.* 55: 9452–9458.

114 Kim, M. and Kim, J. (2014). Redox deposition of birnessite-type manganese oxide on silicon carbide microspheres for use as supercapacitor electrodes. *ACS Appl. Mater. Interfaces* 6: 9036–9045.

115 Pei, L.Z., Tang, Y.H., Chen, Y.W. et al. (2006). Preparation of silicon carbide nanotubes by hydrothermal method. *J. Appl. Phys.* 99: 114306.

116 Raman, V., Bahl, O.P., and Dhawan, U. (1995). Synthesis of silicon carbide through the sol-gel process from different precursors. *J. Mater. Sci.* 30: 2686–2693.

117 Gu, L., Wang, Y., Lu, R. et al. (2015). Silicon carbide nanowires@$Ni(OH)_2$ core-shell structures on carbon fabric for supercapacitor electrodes with excellent rate capability. *J. Power Sources* 273: 479–485.

118 Kim, M., Yoo, Y., and Kim, J. (2014). Synthesis of microsphere silicon carbide/nanoneedle manganese oxide composites and their electrochemical properties as supercapacitors. *J. Power Sources* 265: 214–222.

119 Zhang, H. and Xu, H. (2014). Nanocrystalline silicon carbide thin film electrodes for lithium-ion batteries. *Solid State Ionics* 263: 23–26.

120 Sri Devi Kumari, T., Jeyakumar, D., and Prem Kumar, T. (2013). Nano silicon carbide: a new lithium-insertion anode material on the horizon. *RSC Adv.* 3: 15028–15034.

121 Hu, Y., Liu, X., Zhang, X. et al. (2016). Bead-curtain shaped SiC@SiO_2 core-shell nanowires with superior electrochemical properties for lithium-ion batteries. *Electrochim. Acta* 190: 33–39.
122 Wang, W., Wang, Y., Gu, L. et al. (2015). SiC@Si core-shell nanowires on carbon paper as a hybrid anode for lithium-ion batteries. *J. Power Sources* 293: 492–497.
123 Zang, J., Jia, Y., Pan, H. et al. (2014). Core-shell structured SiC@C supported platinum electrocatalysts for direct methanol fuel cells. *Appl. Catal., B* 144: 166–173.
124 Afsharpourger, M. and Amraee, A.R. (2017). Synthesis of bio-inspired N-doped SiC and investigation of its synergetic effects on Mo catalysts in oxidative desulfurization reaction. *Mol. Catal.* 436: 285–293.